Nonlinear Dyn (2019) 96:885–920
https://doi.org/10.1007/s11071-019-04829-6

ORIGINAL PAPER

Set-valued anisotropic dry friction laws: formulation, experimental verification and instability phenomenon

S. V. Walker · R. I. Leine

Received: 24 September 2018 / Accepted: 6 February 2019 / Published online: 26 February 2019

Abstract Many technical applications, such as brakes and metal forming processes, are affected by anisotropic frictional behavior, where the magnitude and the direction of the friction force are dependent on the sliding direction. Existing dry friction laws do not sufficiently describe all relevant macroscopic aspects of anisotropic friction, and the influence on the dynamics of mechanical systems is largely unknown. Furthermore, previous experimental work on anisotropic friction is limited and the fact that the friction force is not always acting parallel to the sliding direction is often neglected. In this paper, an anisotropic dry friction law with the capability to describe the nonsmooth behavior of stick and slip and allowing for non-convex but star-shaped sets of admissible friction forces is formulated using tools from convex analysis. The formulation of the friction law as normal cone inclusion enables the direct implementation in numerical time-stepping schemes. The stability of systems with anisotropic friction is studied and an eigenvalue analysis reveals that the anisotropic friction law is in theory capable of causing anisotropic friction-induced instability. In addition, experimental setups for detailed investigations of the frictional behavior are described. The measurements reveal complex shaped force reservoirs and confirm the validity of the presented friction law. Finally, it is shown that the presented friction law leads to a more accurate prediction of the motion of nonsmooth mechanical systems.

Keywords Contact · Friction · Anisotropy · Stability

S. V. Walker (✉) · R. I. Leine
Institute for Nonlinear Mechanics, University of Stuttgart, Pfaffenwaldring 9, 70569 Stuttgart, Germany
e-mail: walker@inm.uni-stuttgart.de

R. I. Leine
e-mail: leine@inm.uni-stuttgart.de

1 Introduction

In this work, a set-valued anisotropic dry friction law that enables the use of non-convex friction force reservoirs and allows for an accurate representation of the behavior of stick and slip is formulated in the framework of convex analysis. In addition, experiments are performed to verify the friction law and anisotropic friction is identified as a possible cause of friction-induced instability.

While friction is indispensable in many everyday situations and technical applications such as screws, braking systems, clutches and driving wheels, it often causes unwanted effects in engineering and a large amount of effort is put into the control and reduction of friction forces. The most basic *laws of friction* in use today are commonly attributed to Amontons and Coulomb (see [1] and [2]) and read as:

- The friction force is directly proportional to the normal load.
- The friction force does not depend on the apparent area of contact.

– The friction force is independent of the magnitude of the velocity once motion starts.

The work of tribologists has been focused on extending the friction laws to address different aspects of friction especially on the microscale [3]. For many applications, only the macroscopic aspect of friction is of interest, and the laws of Amontons and Coulomb adequately describe the frictional behavior, which is why they are frequently implemented in multibody simulations. To facilitate a numerical treatment, often regularized friction laws are applied [4]. These regularizations are based on smooth approximations of the discontinuous behavior of the friction force at the transition from slip to stick. Commonly, arctangent functions are used to describe the friction force as a smooth single-valued function of the sliding velocity. The system is then described by an ordinary differential equation and standard integration techniques can be applied. However, regularized friction laws lead to stiff differential equations that cause numerical difficulties and lack the ability to properly describe stiction since even for small nonzero external forces motion is initiated. This motivates the use of set-valued force laws [5] that allow the friction force to take a range of values at zero sliding velocity. The nonsmooth transition from slip to stick involves a discontinuity in the time evolution of the friction force, while the state of the system remains continuous. Such a behavior can be described by extending the differential equation to a differential inclusion with set-valued right-hand side [6]. The framework of this formulation is given by convex and nonsmooth analysis (see [7–10]). Systems with unilateral contact and frictional impacts can be formulated as measure differential inclusions [11,12]. This formulation gives rise to a numerical discretisation known as the time-stepping method [12–14].

Typically, isotropic frictional properties are assumed, in the sense that the magnitude and direction of the friction force are independent of the sliding direction and the location of the contact point on a surface. In reality, the frictional properties of many surfaces significantly vary along different directions of a surface. This anisotropic frictional behavior can be induced by the crystal structure of a material, occurs on the surface of biological, composite or textile materials and may result from machining or finishing of a surface [15]. In engineering, knowledge of anisotropic friction is essential since the majority of engineering surfaces has such properties. Machined surfaces, created, e.g., by cutting, milling or grinding, have a distinct surface pattern which determines frictional behavior [16]. In sheet metal forming, the rolling direction of the material has an influence on the friction forces between the workpiece and the tool which in turn influences the deformation of the workpiece and the surface finish of the product [17,18]. Early experiments specifically performed to study directional effects of friction on metallic surfaces have been carried out by Rabinowicz [19] and Halaunbrenner [20]. Their results indicate that the magnitude of the friction force is dependent on the direction of sliding and the friction force is not always acting parallel to the sliding direction. This is confirmed by the experiments in [21] and [22], where anisotropy results from a macroscopic periodical waviness of the surface. Knowledge of both the magnitude of the friction force and the relationship between the sliding direction and the direction of the friction force is crucial for accurate simulations of systems with anisotropic dry friction.

Different approaches on the modeling of anisotropic dry friction exist. In [23] sliders with wheels or skates are used to model anisotropic frictional behavior. In contrast, in [24] and [25], the microstructure of the contact surface is modeled with unidirectional wedge-shaped asperities, which on the macroscopic scale leads to friction laws similar to laws in plasticity theory. The resulting sets of all friction forces are not necessarily convex, but for convex shapes a bipotential [26] can be applied for finite element computations of systems with anisotropic friction [27]. Furthermore, tensor formulations of anisotropic friction laws exist (see [28] and [29]) and the concept of normal cone inclusions has been applied, e.g., for the simulation of a snake robot [30] and a bobsleigh [31].

Another important aspect of mechanical systems with friction is the possible occurrence of friction-induced instabilities. The squealing of automotive braking systems is one of the most prominent examples demonstrating the loss of stability of a steady sliding motion. Many other examples can be found in technical applications, where the loss of stability often occurs due to friction-induced Hopf bifurcations. Despite the fact that many researchers have extensively studied the field of friction-induced vibrations, the underlying mechanisms are still not fully understood. Especially, the influence of anisotropic friction on the stability of slid-

ing motion has not been studied yet. In [32] a historical review of the stick-slip phenomenon is given. In addition to stick-slip, in [33] possible mechanisms leading to chatter are described. The effects of sprag-slip and mode-coupling are described, e.g., in [34] and [35], respectively. The surveys [36–39] review the classical friction models used to represent the frictional behavior in braking systems. Furthermore, in [40], an in-depth study of the stability of systems with friction and brake squeal in particular is given.

From the existing literature in the field of anisotropic dry friction, several unsolved problems can be identified:

- No existing dry friction law sufficiently describes all relevant macroscopic aspects of anisotropic frictional behavior and is formulated such that it allows for an implementation in numerical time-stepping schemes.
- The influence of anisotropic friction on the stability of equilibria of mechanical systems is unknown.
- Previous experimental work on anisotropic friction is insufficient.

A fundamental criterion of a meaningful dry friction law is the accurate description of the constitutive behavior of stick and slip, which requires a set-valued formulation. Friction laws given in the form of normal cone inclusions are capable of describing this behavior. However, they are based on the assumptions that the set of all admissible friction forces is convex and the sliding direction is defined by normality to that set. Those assumptions do not necessarily hold for real anisotropic frictional behavior. Most of the existing tribometers and other experimental setups used for the measurement of friction forces only record the component of the friction force directly opposing the sliding direction. Anisotropic friction forces, however, are generally not collinear to the sliding direction. Information on the force component acting orthogonal to the direction of sliding is therefore often lost. To validate anisotropic friction laws, accurate measurement results of the magnitude and direction of the friction as a function of the sliding direction are necessary.

In this paper, the properties of systems with anisotropic dry friction are analyzed analytically as well as experimentally. The paper provides the reader with the mathematical background necessary for the formulation of anisotropic friction laws in the framework of convex analysis and for the numerical simulation with time-stepping methods. Specifically, the aims of this work are:

- To formulate a highly general force law that enables the description of a large class of anisotropic dry friction models and that can be implemented in existing numerical algorithms,
- To classify different isotropic friction-induced instability phenomena according to their underlying mechanisms and to analyze the possibility of anisotropic friction being the cause of self-excited vibrations,
- To experimentally analyze the effects of anisotropic friction both qualitatively and quantitatively.

Throughout this work, in the sense of Amontons, the friction force is assumed to be proportional to the normal load and independent of the apparent area of contact. The scope of this work is the contact between uniform surfaces, i.e., anisotropy due to different friction properties at different locations of a surface is not considered. Furthermore, only the macroscopic behavior of mechanical systems is of interest. Microscopic effects and wear at the contact points are neglected.

Section 2 provides the mathematical preliminaries that are needed in the remainder of this work and the equation of motion of a system with contacts is introduced. Anisotropic friction laws are discussed in Sect. 3. First, associated friction laws that are based on normality of the sliding direction to a convex force reservoir are analyzed. After showing that different friction models lead to force laws in which normality to the force reservoir is no longer given and the force reservoir is not necessarily convex, an extended normal cone inclusion friction law is formulated. Section 4 is concerned with friction-induced instability mechanisms. Two experimental setups are presented in Sect. 5, and experimental results for different contact partners are shown.

2 Nonsmooth dynamics

This section gives a brief introduction to the dynamics of nonsmooth mechanical systems [5,13,41,42]. The nonsmooth nature of systems with unilateral contact or dry friction can be expressed in the framework of convex analysis by means of set-valued force laws.

2.1 Elements from convex analysis

Comprehensive treatises of the topic are given by [7] and [8]. We consider a subset $\mathscr{C}$ of $\mathbb{R}^p$ and denote its boundary and interior, bdry $\mathscr{C}$ and int $\mathscr{C}$, respectively.

Definition 1 (*Convex Set*) A set $\mathscr{C} \subseteq \mathbb{R}^p$ is called *convex* if for every pair of points $\boldsymbol{x} \in \mathscr{C}$ and $\boldsymbol{y} \in \mathscr{C}$ also $(1-s)\boldsymbol{x} + s\boldsymbol{y} \in \mathscr{C}$ for all $s \in (0,1)$. In addition, it is *strictly convex* if $(1-s)\boldsymbol{x} + s\boldsymbol{y} \in \operatorname{int}\mathscr{C}$ for all $s \in (0,1)$.

A special case of possibly non-convex sets are star-shaped sets.

Definition 2 (*Star-Shaped Set*) A set $\mathscr{C} \subseteq \mathbb{R}^p$ is called *star-shaped* with respect to the origin if for every $\boldsymbol{x} \in \mathscr{C}$ also $s\boldsymbol{x} \in \mathscr{C}$ for all $s \in [0,1)$. In addition, it is called *strictly star-shaped* if $s\boldsymbol{x} \in \operatorname{int}\mathscr{C}$ for all $s \in [0,1)$.

Figure 1 shows examples of different sets.

A function $f\colon \mathbb{R}^p \to \mathbb{R} \cup \{\infty\}$ is called convex if its epigraph $\operatorname{epi}(f(\boldsymbol{x})) = \{(\boldsymbol{x}, z) \in \mathbb{R}^p \times \mathbb{R} \mid z \geq f(\boldsymbol{x}),\ \boldsymbol{x} \in \mathbb{R}^p\}$ is a convex subset of $\mathbb{R}^{p+1}$. For a convex but possibly non-differentiable function having the additional properties of being lower semi-continuous and proper [7], the *subdifferential* is defined as

$$\partial f(\boldsymbol{x}) = \left\{\boldsymbol{y} \mid f(\boldsymbol{x}^*) \geq f(\boldsymbol{x}) + \boldsymbol{y}^{\mathrm{T}}(\boldsymbol{x}^* - \boldsymbol{x}),\ \forall \boldsymbol{x}^* \in \mathbb{R}^p\right\}. \tag{1}$$

The subdifferential is a set-valued function, $\partial f(\boldsymbol{x})\colon \mathbb{R}^p \rightrightarrows \mathbb{R}^p$. An example is given by the set-valued Sign function being defined by

$$\operatorname{Sign}(x) = \partial|x| = \begin{cases} -1 & \text{for } x < 0, \\ [-1,1] & \text{for } x = 0, \\ 1 & \text{for } x > 0. \end{cases} \tag{2}$$

Definition 3 (*Gauge Function*) Let $\mathscr{C} \subseteq \mathbb{R}^p$ be closed and star-shaped with respect to the origin. The *gauge function* of $\mathscr{C}$ is defined as $k_{\mathscr{C}}(\boldsymbol{x}) = \inf\{s > 0 \mid \boldsymbol{x} \in s\mathscr{C}\}$.

It follows that the set $\mathscr{C}$ in Definition 3 is given as level set of the gauge function, i.e., $\mathscr{C} = \{\boldsymbol{x} \in \mathbb{R}^p \mid k_{\mathscr{C}}(\boldsymbol{x}) \leq 1\}$. Gauge functions are defined for star-shaped sets and are nonnegative and positively homogeneous functions of degree one [43] as illustrated in Fig. 2a.

Definition 4 (*Indicator Function*) The *indicator function* of the set $\mathscr{C}$ is defined as

$$\Psi_{\mathscr{C}}(\boldsymbol{x}) = \begin{cases} 0 & \text{for } \boldsymbol{x} \in \mathscr{C}, \\ +\infty & \text{for } \boldsymbol{x} \notin \mathscr{C}. \end{cases} \tag{3}$$

The gauge as well as the indicator function of a set $\mathscr{C}$ are convex if and only if the set $\mathscr{C}$ is convex.

The *convex conjugate* f^* of a convex function f is defined as

$$f^*(\boldsymbol{x}^*) = \sup_{\boldsymbol{x}} \left\{\boldsymbol{x}^{\mathrm{T}}\boldsymbol{x}^* - f(\boldsymbol{x})\right\}. \tag{4}$$

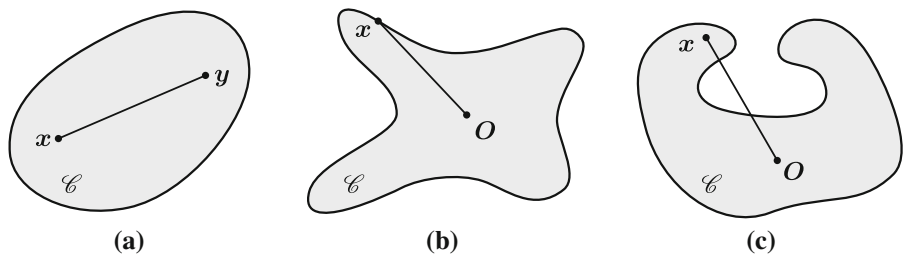

Fig. 1 **a** Convex set, **b** star-shaped and **c** not star-shaped set

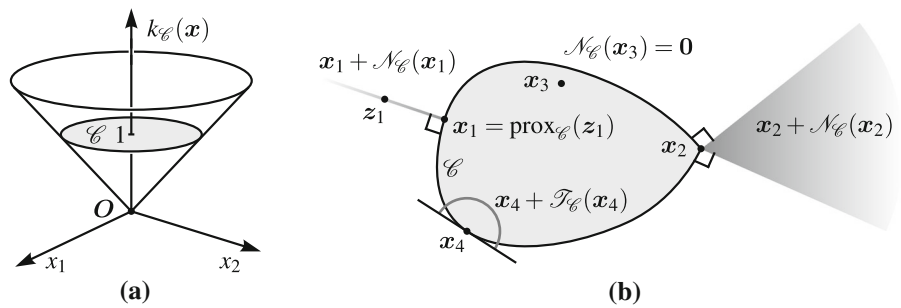

Fig. 2 **a** Gauge function $k_{\mathscr{C}}$ and level set $\mathscr{C}$, **b** convex set $\mathscr{C}$ with normal cone, proximal point and tangent cone

For proper, lower semi-continuous and convex functions, it holds that the Fenchel equality

$$\boldsymbol{x}^{\mathrm{T}}\boldsymbol{x}^* = f(\boldsymbol{x}) + f^*(\boldsymbol{x}^*) \iff \boldsymbol{x}^* \in \partial f(\boldsymbol{x}) \iff \boldsymbol{x} \in \partial f(\boldsymbol{x}^*) \tag{5}$$

is fulfilled. Of particular importance is the convex conjugate of the indicator function, which is called support function.

Definition 5 (*Support Function*) Let $\mathscr{C} \subseteq \mathbb{R}^p$ be closed and convex. The *support function* of $\mathscr{C}$ is given as

$$\Psi^*_{\mathscr{C}}(\boldsymbol{x}^*) = \sup_{\boldsymbol{x}} \left\{ \boldsymbol{x}^{\mathrm{T}}\boldsymbol{x}^* \mid \boldsymbol{x} \in \mathscr{C} \right\}. \tag{6}$$

In this work, normal cone inclusions are of special interest since they allow for the formulation of set-valued force laws.

Definition 6 (*Normal Cone*) Let $\mathscr{C} \subseteq \mathbb{R}^p$ be closed, nonempty and convex and let $\boldsymbol{x} \in \mathscr{C}$. The set of all vectors $\boldsymbol{y} \in \mathbb{R}^p$ which do not make an acute angle with any vector $\boldsymbol{x} - \boldsymbol{x}^*$ for all $\boldsymbol{x}^* \in \mathscr{C}$ form the *normal cone* of $\mathscr{C}$ in $\boldsymbol{x}$,

$$\mathscr{N}_{\mathscr{C}}(\boldsymbol{x}) = \left\{ \boldsymbol{y} \mid \boldsymbol{y}^{\mathrm{T}}(\boldsymbol{x}^* - \boldsymbol{x}) \leq 0,\ \boldsymbol{x} \in \mathscr{C},\ \forall \boldsymbol{x}^* \in \mathscr{C} \right\}. \tag{7}$$

For $\boldsymbol{x} \notin \mathscr{C}$, it holds that $\mathscr{N}_{\mathscr{C}}(\boldsymbol{x}) = \emptyset$. The subdifferential of the indicator function yields exactly the definition of the normal cone, i.e.,

$$\partial \Psi_{\mathscr{C}}(\boldsymbol{x}) = \mathscr{N}_{\mathscr{C}}(\boldsymbol{x}). \tag{8}$$

For a nonsingular linear mapping $\boldsymbol{A} \in \mathbb{R}^{p\times p}$, the transformation property

$$\boldsymbol{y} \in \mathscr{N}_{\mathscr{C}}(\boldsymbol{x}) \iff \boldsymbol{A}^{\mathrm{T}}\boldsymbol{y} \in \mathscr{N}_{\boldsymbol{A}^{-1}\mathscr{C}}(\boldsymbol{A}^{-1}\boldsymbol{x}) \tag{9}$$

follows from the chain rule of convex analysis [41,44]. The transformed set $\boldsymbol{A}^{-1}\mathscr{C}$ consists of all the vectors z with $\boldsymbol{A}z \in \mathscr{C}$.

In addition to the normal cone, the tangent cone [45] and proximal point function can be defined as follows.

Definition 7 (*Tangent Cone*) Let $\mathscr{C} \subseteq \mathbb{R}^p$ be closed and let $\boldsymbol{x} \in \mathscr{C}$. The *tangent cone* of $\mathscr{C}$ in $\boldsymbol{x}$ is defined as

$$\mathscr{T}_{\mathscr{C}}(\boldsymbol{x}) = \{ \boldsymbol{y} \mid \forall t_k \downarrow 0,\ \boldsymbol{x}_k \to \boldsymbol{x} \text{ with } \boldsymbol{x}_k \in \mathscr{C}, \exists \boldsymbol{y}_k \to \boldsymbol{y} \text{ with } \boldsymbol{x}_k + t_k \boldsymbol{y}_k \in \mathscr{C} \}. \tag{10}$$

Definition 8 (*Proximal Point Function*) Let $\mathscr{C} \subseteq \mathbb{R}^p$ be closed, nonempty and convex. The *proximal point function* $\mathrm{prox}_{\mathscr{C}}(z)$ determines the closest point to z in $\mathscr{C}$,

$$\mathrm{prox}_{\mathscr{C}}(z) = \operatorname*{argmin}_{\boldsymbol{x}^* \in \mathscr{C}} \|z - \boldsymbol{x}^*\|, \quad z \in \mathbb{R}^p. \tag{11}$$

The notation $\mathrm{prox}_{\mathscr{C}}(z)$ has been used here to denote a projection on a closed convex set, see [12], and has not to be confused with the proximal operator associated with a convex function. Normal cone inclusions can be rewritten as implicit equations using proximal point functions. It holds that

$$\boldsymbol{y} \in \mathscr{N}_{\mathscr{C}}(\boldsymbol{x}) \iff \boldsymbol{x} = \mathrm{prox}_{\mathscr{C}}(\boldsymbol{x} + r\boldsymbol{y}), \quad r > 0. \tag{12}$$

In Fig. 2b, normal and tangent cones as well as the relationship between the normal cone and the proximal point function are illustrated for a two-dimensional set.

The proximal point function $\boldsymbol{x} = \mathrm{prox}_{\mathscr{C}}(z)$ yields $\boldsymbol{x} = z$ if $z \in \mathscr{C}$. For a point $z \notin \mathscr{C}$, the proximal point function results in a projection of z on the boundary of the set $\mathscr{C}$. For convex sets having a smooth boundary, i.e., the gradient of the gauge function $k_{\mathscr{C}}(\boldsymbol{x})$ exists for all $\boldsymbol{x} \neq \boldsymbol{0}$, it holds that

$$\boldsymbol{x} = \mathrm{prox}_{\mathscr{C}}(z) \iff \boldsymbol{x} + \beta \nabla k_{\mathscr{C}}(\boldsymbol{x}) = z, \quad \text{with } \beta > 0. \tag{13}$$

In addition, the condition $k_{\mathscr{C}}(\boldsymbol{x}) = 1$ must be fulfilled since the projected point $\boldsymbol{x}$ has to be on the boundary of $\mathscr{C}$. This set of equations allows for the calculation of the closest point to z in $\mathscr{C}$.

2.2 Equation of motion

The dynamics of a time-autonomous mechanical system with n degrees of freedom and no frictional unilateral constraints can be described by the equation of motion

$$\boldsymbol{M}(\boldsymbol{q})\ddot{\boldsymbol{q}} - \boldsymbol{h}(\boldsymbol{q}, \dot{\boldsymbol{q}}) = \boldsymbol{0}, \tag{14}$$

where $\boldsymbol{q} = \boldsymbol{q}(t) \in \mathbb{R}^n$ denotes the time dependent set of generalized coordinates, $\boldsymbol{M} \in \mathbb{R}^{n\times n}$ is the symmetric

and positive definite mass matrix and the vector $\boldsymbol{h} \in \mathbb{R}^n$ contains all differentiable forces and gyroscopic terms. The restriction to time-autonomous systems is not essential, but is made in this work for simplicity. If, in addition, m normal and frictional contact forces act on the system, the equation of motion can be extended as

$$\boldsymbol{M}(\boldsymbol{q})\dot{\boldsymbol{u}} - \boldsymbol{h}(\boldsymbol{q},\boldsymbol{u}) = \sum_{i=1}^{m} \left(\boldsymbol{w}_{Ni}(\boldsymbol{q})\lambda_{Ni} + \boldsymbol{W}_i(\boldsymbol{q})\boldsymbol{\lambda}_i\right), \tag{15}$$

where the generalized velocities are denoted $\boldsymbol{u}$, and $\boldsymbol{u} = \dot{\boldsymbol{q}}$ holds for almost all t. The normal force at contact point i is called $\lambda_{Ni} \in \mathbb{R}$ and $\boldsymbol{\lambda}_i \in \mathbb{R}^p$ is the corresponding friction force. The dimension p of the friction force may vary depending on the considered system. For instance, for planar mechanical systems the sliding friction force is scalar ($p = 1$). For spatial mechanical systems, the contacting bodies have a contact plane and the sliding friction force is two-dimensional (see Sect. 3.1). Higher dimensions are necessary if combined sliding and drilling or rolling friction is considered [42]. The generalized force directions of the normal and friction force are defined by $\boldsymbol{w}_{Ni} \in \mathbb{R}^n$ and $\boldsymbol{W}_i \in \mathbb{R}^{n\times p}$.

The contact forces and force directions are assembled in the vectors and matrices $\boldsymbol{\lambda}_N, \boldsymbol{\lambda}, \boldsymbol{W}_N, \boldsymbol{W}$ and the equation of motion can be rewritten in the form

$$\boldsymbol{M}(\boldsymbol{q})\dot{\boldsymbol{u}} - \boldsymbol{h}(\boldsymbol{q},\boldsymbol{u}) = \boldsymbol{W}_N(\boldsymbol{q})\boldsymbol{\lambda}_N + \boldsymbol{W}(\boldsymbol{q})\boldsymbol{\lambda}. \tag{16}$$

Note that whenever sliding friction in particular is considered, i.e., without additional drilling or rolling friction, the index $_T$ is added to the friction force and generalized force direction yielding $\boldsymbol{\lambda}_T$ and $\boldsymbol{W}_T$. In this work, motion without impacts is considered. Therefore, the generalized coordinates $\boldsymbol{q}(t)$ as well as the velocities $\boldsymbol{u}(t)$ are assumed to be time-continuous functions. However, when a transition from slip to stick occurs or when the direction of sliding at a contact point is reversed, the friction force $\boldsymbol{\lambda}(t)$ is discontinuous. At such time instants, the generalized accelerations $\dot{\boldsymbol{u}}$ are not defined. Equation (16) therefore only holds for almost all t.

2.3 Time-stepping method

The equation of motion Eq. (16) of a mechanical system with contact points in combination with set-valued force laws, given, e.g., in the form of normal cone inclusions, yields a differential inclusion. Numerical integration of nonsmooth systems is possible with event-driven or time-stepping methods. In the following, the time-stepping method developed by [12] is briefly described.

The equation of motion can be replaced by the equality of measures

$$\boldsymbol{M}\mathrm{d}\boldsymbol{u} - \boldsymbol{h}\mathrm{d}t = \boldsymbol{W}_N\mathrm{d}\boldsymbol{P}_N + \boldsymbol{W}\mathrm{d}\boldsymbol{P}, \tag{17}$$

where the dependence of the terms on $\boldsymbol{q}$ and $\boldsymbol{u}$ is omitted for brevity. This formulation allows for the occurrence of impacts. In this work, impacts are not considered and the differential measures are given by $\mathrm{d}\boldsymbol{u} = \dot{\boldsymbol{u}}\mathrm{d}t$, $\mathrm{d}\boldsymbol{P}_N = \boldsymbol{\lambda}_N\mathrm{d}t$ and $\mathrm{d}\boldsymbol{P} = \boldsymbol{\lambda}\mathrm{d}t$. Since the set of time instants for which the acceleration $\dot{\boldsymbol{u}}$ does not exist is Lebesgue negligible [42], the time evolution of the velocity $\boldsymbol{u}$ is given by

$$\boldsymbol{u}(t) = \boldsymbol{u}(t_0) + \int_{t_0}^{t} \mathrm{d}\boldsymbol{u} \quad \forall t \geq t_0. \tag{18}$$

In Moreau's time-stepping scheme, the equality of measures is approximated over small time steps Δt. The subscripts $_\mathrm{B}$, $_\mathrm{M}$ and $_\mathrm{E}$ are used to describe values at the beginning, midpoint and end of a time step, respectively. The generalized coordinates and velocities at the beginning of a time step, $\boldsymbol{q}_\mathrm{B}$ and $\boldsymbol{u}_\mathrm{B}$, are known and the coordinates at the midpoint are obtained from $\boldsymbol{q}_\mathrm{M} = \boldsymbol{q}_\mathrm{B} + \frac{1}{2}\boldsymbol{u}_\mathrm{B}\Delta t$. System matrices and vectors evaluated at the midpoint are denoted with a subscript $_\mathrm{M}$. For closed contacts at the midpoint, the inclusion problem

$$\begin{aligned} &\boldsymbol{M}_\mathrm{M}(\boldsymbol{u}_\mathrm{E} - \boldsymbol{u}_\mathrm{B}) - \boldsymbol{h}_\mathrm{M}\Delta t = \boldsymbol{W}_{N\mathrm{M}}\boldsymbol{P}_N + \boldsymbol{W}_\mathrm{M}\boldsymbol{P}, \\ &\boldsymbol{\gamma}_{N\mathrm{E}} \in \mathscr{N}_{\mathbb{R}_0^-}(-\boldsymbol{P}_N), \quad \boldsymbol{\gamma}_\mathrm{E} \in \mathscr{N}_{\mathscr{C}(\boldsymbol{P}_N)}(-\boldsymbol{P}) \end{aligned} \tag{19}$$

needs to be solved for the velocities $\boldsymbol{u}_\mathrm{E}$ at the end of the time step, where the set-valued force laws are formulated in terms of the normal and frictional contact efforts, $\boldsymbol{P}_N$ and $\boldsymbol{P}$. Using Eq. (12), normal cone inclusions can be rewritten as implicit proximal point functions. This allows for an iterative solution of the contact problem, e.g., with a modified Newton algorithm [46]. The scheme

$$\boldsymbol{u}_\mathrm{E}^k = \boldsymbol{u}_\mathrm{B} + \boldsymbol{M}_\mathrm{M}^{-1}\left(\boldsymbol{h}_\mathrm{M}\Delta t + \boldsymbol{W}_{N\mathrm{M}}\boldsymbol{P}_N^k + \boldsymbol{W}_\mathrm{M}\boldsymbol{P}^k\right), \tag{20}$$

$$\boldsymbol{P}_N^{k+1} = -\operatorname{prox}_{\mathbb{R}_0^-}\left(-\boldsymbol{P}_N^k + r_N \boldsymbol{\gamma}_{N\mathrm{E}}^k\right), \quad r_N > 0, \tag{21}$$

$$\boldsymbol{P}^{k+1} = -\operatorname{prox}_{\mathscr{C}\left(\boldsymbol{P}_N^{k+1}\right)}\left(-\boldsymbol{P}^k + r\boldsymbol{\gamma}_{\mathrm{E}}^k\right), \quad r > 0 \tag{22}$$

is iterated with an initial guess of the contact efforts, until a stopping criterion is reached. The relative velocities are given as

$$\boldsymbol{\gamma}_{N\mathrm{E}}^k = \boldsymbol{W}_{N\mathrm{M}}^{\mathrm{T}} \boldsymbol{u}_{\mathrm{E}}^k \quad \text{and} \quad \boldsymbol{\gamma}_{\mathrm{E}}^k = \boldsymbol{W}_{\mathrm{M}}^{\mathrm{T}} \boldsymbol{u}_{\mathrm{E}}^k + \boldsymbol{\chi}. \tag{23}$$

Finally, the coordinates $\boldsymbol{q}_{\mathrm{E}}$ at the end of the time step can be calculated by $\boldsymbol{q}_{\mathrm{E}} = \boldsymbol{q}_{\mathrm{M}} + \frac{1}{2}\boldsymbol{u}_{\mathrm{E}} \Delta t$.

3 Anisotropic friction force laws

In the following, $\boldsymbol{\lambda} \in \mathbb{R}^p$ describes the friction force and $\boldsymbol{\gamma} \in \mathbb{R}^p$ the relative velocity between two contacting bodies. In the case of combined sliding and drilling or rolling friction, $\boldsymbol{\gamma}$ contains the tangential sliding velocity and the spin of the contacting bodies scaled to a velocity. The normal force at the contact is supposed to be known and is called λ_N. In the sense of Amontons, friction forces are assumed to be directly proportional to the normal force. The dependence of the friction force on the normal force is not written explicitly.

Definition 9 (*Dry Friction Law*) Let $\mathscr{F} : \mathbb{R}^p \rightrightarrows \mathbb{R}^p$ be an upper semi-continuous set-valued function and let the image of $\mathscr{F}(\boldsymbol{\gamma})$ be a compact set for all fixed values of $\boldsymbol{\gamma}$ and a star-shaped set with respect to the origin for $\boldsymbol{\gamma} = \boldsymbol{0}$ with $\mathscr{F}(\boldsymbol{0}) \neq \{\boldsymbol{0}\}$. A *dry friction law* connects the relative sliding velocity to the friction force via

$$-\boldsymbol{\lambda} \in \mathscr{F}(\boldsymbol{\gamma}). \tag{24}$$

A dry friction law is characterized by having a stick phase, i.e., the friction force has for zero relative velocity the character of a constraint force. Hence, a dry friction law allows for a nonzero friction force at zero relative velocity (stick).

In the following, friction laws are considered where no dependence on the magnitude of the sliding velocity is assumed to exist, as stated by Coulomb. Coulomb-type friction laws are defined based on Definition 9 of dry friction laws.

Definition 10 (*Coulomb-Type Friction Law*) A dry friction law is called *Coulomb-type friction law* if it holds that

$$\mathscr{F}(\boldsymbol{\gamma}) = \mathscr{F}(a\boldsymbol{\gamma}) \quad \forall a \in \mathbb{R}^+. \tag{25}$$

Hence, the magnitude of the sliding velocity has no influence on the flow rule.

The set of all admissible friction forces $\mathscr{C} \subset \mathbb{R}^p$ is called *force reservoir*. It holds that $\mathscr{F}(\boldsymbol{\gamma}) \subseteq \mathscr{C}$ and $-\boldsymbol{\lambda} \in \mathscr{C}$. During stick, the force reservoir $\mathscr{C}$ and the image of $\mathscr{F}(\boldsymbol{0})$ coincide, i.e., $\mathscr{C} = \mathscr{F}(\boldsymbol{0})$. Since the image of $\mathscr{F}(\boldsymbol{\gamma})$ is compact for all $\boldsymbol{\gamma}$ and star-shaped for $\boldsymbol{\gamma} = \boldsymbol{0}$, the force reservoir has the same properties. A bounded force reservoir excludes friction forces with an infinite magnitude which would completely prevent sliding in the corresponding direction, e.g., a one-way clutch. Force reservoirs that are not star-shaped are not suitable to describe the stick phase. Consider a body under an external load being in static equilibrium such that the negative friction force equals the external load. If the magnitude of the external load is reduced, the body remains in the stick phase and the magnitude of the friction force reduces correspondingly. This is impossible for a force reservoir that is not star-shaped with respect to the origin as seen in Fig. 3a since friction forces with a smaller magnitude are not always part of the force reservoir.

During slip, the friction force is defined by the possibly set-valued *flow rule* $\mathscr{F}(\boldsymbol{\gamma})$ with $\boldsymbol{\gamma} \neq \boldsymbol{0}$. A fundamental requirement for a physically meaningful friction force law is that the friction force does not create energy in the system. Let the rate of dissipation $D(-\boldsymbol{\lambda}, \boldsymbol{\gamma})$ be given by

$$D(-\boldsymbol{\lambda}, \boldsymbol{\gamma}) = -\boldsymbol{\lambda}^{\mathrm{T}}\boldsymbol{\gamma} \quad \text{with} \quad -\boldsymbol{\lambda} \in \mathscr{F}(\boldsymbol{\gamma}). \tag{26}$$

During stick, $D(-\boldsymbol{\lambda}, \boldsymbol{0}) = 0$. If $\mathscr{F}(\boldsymbol{\gamma})$ is single-valued for $\boldsymbol{\gamma} \neq \boldsymbol{0}$, then the rate of dissipation is solely a function of the sliding velocity and we write $D(\boldsymbol{\gamma})$. The same holds if the function is multi-valued if for a fixed $\boldsymbol{\gamma}$ the condition $-\boldsymbol{\lambda}^{\mathrm{T}}\boldsymbol{\gamma} = \text{const.}$ is fulfilled for all $-\boldsymbol{\lambda} \in \mathscr{F}(\boldsymbol{\gamma})$. This case is illustrated in Fig. 3b.

Definition 11 (*Dissipativity of Dry Friction Law*) A dry friction law is called

(i) *dissipative* if

$$D(-\boldsymbol{\lambda}, \boldsymbol{\gamma}) \geq 0 \quad \forall \boldsymbol{\gamma} \quad \forall -\boldsymbol{\lambda} \in \mathscr{F}(\boldsymbol{\gamma}),$$

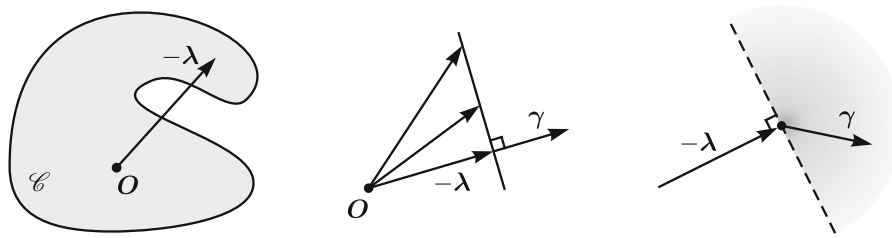

Fig. 3 **a** Not star-shaped and therefore nonadmissible friction force reservoir. **b** Constant rate of dissipation for different friction forces $\boldsymbol{\lambda}$. **c** Range of admissible sliding directions for a given $\boldsymbol{\lambda}$

(ii) *strictly dissipative* if

$$D(-\boldsymbol{\lambda}, \boldsymbol{\gamma}) > 0 \quad \forall \boldsymbol{\gamma} \neq \mathbf{0} \quad \forall -\boldsymbol{\lambda} \in \mathscr{F}(\boldsymbol{\gamma}).$$

Figure 3c shows a graphical representation of the admissible sliding directions for a specific friction force for dissipative friction laws. In the following, restrictions on the relationship between the sliding velocity and the friction force and on the force reservoir are given.

Definition 12 (*Associated Coulomb Friction Law*) Let the set $\mathscr{C} \subset \mathbb{R}^p$ be nonempty, compact and convex. A Coulomb-type friction law is called *associated* if $\mathscr{F}(\boldsymbol{\gamma}) = \partial \Psi^*_{\mathscr{C}}(\boldsymbol{\gamma})$, i.e.,

$$-\boldsymbol{\lambda} \in \partial \Psi^*_{\mathscr{C}}(\boldsymbol{\gamma}) \iff \boldsymbol{\gamma} \in \mathscr{N}_{\mathscr{C}}(-\boldsymbol{\lambda}). \tag{27}$$

The associated friction law is thus defined by normality of the sliding velocity $\boldsymbol{\gamma}$ to the boundary of the force reservoir during slip. For all friction forces in the interior of the force reservoir, the contacting bodies stick and the relative sliding velocity is zero. This behavior is described by the normal cone inclusion where the sliding velocity is in the normal cone $\mathscr{N}_{\mathscr{C}}(\boldsymbol{\gamma})$ to the force reservoir $\mathscr{C}$.

The inverse relation of the normal cone inclusion is the friction force being in the subdifferential of the support function of the force reservoir $\Psi^*_{\mathscr{C}}(\boldsymbol{\gamma})$. It is derived using the Fenchel equality Eq. (5) and the fact that the subdifferential of the indicator function of a convex set is the normal cone to the set.

Proposition 1 (Dissipativity of Associated Coulomb Friction Law) *An associated Coulomb friction law is dissipative. It is even strictly dissipative if* $\mathbf{0} \in \operatorname{int} \mathscr{C}$ *for all* $\boldsymbol{\gamma}$.

Proof From the definition of the rate of dissipation Eq. (26) and the Fenchel equality Eq. (5), it follows that

$$D(-\boldsymbol{\lambda}, \boldsymbol{\gamma}) = -\boldsymbol{\lambda}^{\mathrm{T}} \boldsymbol{\gamma} = \Psi_{\mathscr{C}}(-\boldsymbol{\lambda}) + \Psi^*_{\mathscr{C}}(\boldsymbol{\gamma}). \tag{28}$$

The indicator function $\Psi_{\mathscr{C}}(-\boldsymbol{\lambda})$ vanishes since the friction force is always in the force reservoir. It follows that the rate of dissipation is only a function of the sliding velocity. Because the force reservoir must contain the origin, the support function is nonnegative [42] which gives

$$D(\boldsymbol{\gamma}) = \Psi^*_{\mathscr{C}}(\boldsymbol{\gamma}) \geq 0. \tag{29}$$

In addition, if $\mathbf{0} \in \operatorname{int} \mathscr{C}$, the support function is strictly positive, $\Psi^*_{\mathscr{C}}(\boldsymbol{\gamma}) > 0$ for all $\boldsymbol{\gamma} \neq \mathbf{0}$. □

Next, we consider the principle of maximum dissipation introduced in [47].

Proposition 2 (Principle of Maximum Dissipation) *For a given compact and convex force reservoir* $\mathscr{C}$*, the flow rule which maximizes the rate of dissipation is the associated flow rule.*

Proof Let the friction force during slip ($\boldsymbol{\gamma} \neq \mathbf{0}$) be given by the flow rule $-\boldsymbol{\lambda} \in \mathscr{F}(\boldsymbol{\gamma})$ such that the rate of dissipation yields

$$D(-\boldsymbol{\lambda}, \boldsymbol{\gamma}) = -\boldsymbol{\lambda}^{\mathrm{T}} \boldsymbol{\gamma} \geq -\boldsymbol{\lambda}^{*\mathrm{T}} \boldsymbol{\gamma} \quad \forall \boldsymbol{\gamma} \; \forall -\boldsymbol{\lambda} \in \mathscr{F}(\boldsymbol{\gamma}) \tag{30}$$

for all other flow rules $-\boldsymbol{\lambda}^* \in \mathscr{F}^*(\boldsymbol{\gamma})$ with $-\boldsymbol{\lambda}^* \in \mathscr{C}$. Rewriting Eq. (30) results in the definition of a normal cone (see Definition 6),

$$-(\boldsymbol{\lambda} - \boldsymbol{\lambda}^*)^{\mathrm{T}} \boldsymbol{\gamma} \geq 0 \quad \forall -\boldsymbol{\lambda}^* \in \mathscr{C} \implies \boldsymbol{\gamma} \in \mathscr{N}_{\mathscr{C}}(-\boldsymbol{\lambda}). \tag{31}$$

Therefore, if the principle of maximum dissipation is assumed to hold, then the associated flow rule is obtained. □

Definition 13 (*Maximal Monotone Coulomb-Type Friction Law*) A Coulomb-type friction law is called *maximal monotone* if $\mathscr{F}(\boldsymbol{\gamma})$ is maximal monotone, i.e.,

(i) $\forall(\boldsymbol{\gamma}, -\boldsymbol{\lambda}) \in \mathrm{Graph}(\mathscr{F}),\ \forall(\boldsymbol{\gamma}^*, -\boldsymbol{\lambda}^*) \in \mathrm{Graph}(\mathscr{F}),$
$\Longrightarrow\ -(\boldsymbol{\lambda} - \boldsymbol{\lambda}^*)^{\mathrm{T}}(\boldsymbol{\gamma} - \boldsymbol{\gamma}^*) \geq 0,$

(ii) $\mathrm{Graph}(\mathscr{F}) \subseteq \mathrm{Graph}(\hat{\mathscr{F}}) \Longrightarrow \mathrm{Graph}(\mathscr{F}) = \mathrm{Graph}(\hat{\mathscr{F}})$ for all functions $\hat{\mathscr{F}}$ fulfilling Condition (i).

Definition 13(i) ensures the monotonicity of $\mathscr{F}$, while Condition(ii) (see [48]) adds that $\mathscr{F}$ is called maximal monotone if there exists no other monotone set-valued function whose graph strictly contains the graph of $\mathscr{F}$. In other words, no enlargement of the graph is possible without destroying the monotonicity of $\mathscr{F}$ [8].

Proposition 3 *Every maximal monotone Coulomb-type friction law is an associated Coulomb friction law.*

Proof Substitution of $\boldsymbol{\gamma}^* = \mathbf{0}$ in the definition of monotonicity (Definition 13(i)) leads to the definition of a normal cone, i.e.,

$$-(\boldsymbol{\lambda} - \boldsymbol{\lambda}^*)^{\mathrm{T}}\boldsymbol{\gamma} \geq 0 \quad \forall -\boldsymbol{\lambda}^* \in \mathscr{C} \implies \boldsymbol{\gamma} \in \mathscr{N}_{\mathscr{C}}(-\boldsymbol{\lambda}).$$

□

Therefore, for a given force reservoir, the only existing maximal monotone Coulomb-type friction law is the associated Coulomb friction law. Vice versa, the following proposition holds.

Proposition 4 *Every associated Coulomb friction law is maximal monotone.*

Proof For associated Coulomb friction laws it holds that $\mathscr{F}(\boldsymbol{\gamma}) = \partial\Psi^*_{\mathscr{C}}(\boldsymbol{\gamma})$. The support function $\Psi^*_{\mathscr{C}}(\boldsymbol{\gamma})$ is a lower semi-continuous convex function. The subdifferential of such a function is maximal monotone [7]. □

Hence, maximal monotone Coulomb-type friction laws are exactly associated Coulomb friction laws.

Let a system be described by a differential inclusion consisting of the equation of motion together with a set-valued associated Coulomb friction law. From the maximal monotonicity of $\mathscr{F}(\boldsymbol{\gamma})$, existence and uniqueness of solutions follows [42].

3.1 Planar friction

The definitions and propositions formulated above are valid in $\mathbb{R}^p$. If tangential friction forces in a contact plane are considered, then p is equal to two. Higher dimensions are necessary if in addition to sliding friction forces a friction torque due to combined sliding and drilling or rolling motion occurs [42,49]. In the following sections, sliding in the tangential contact plane spanned by $\mathbf{e}_{T_1}$ and $\mathbf{e}_{T_2}$ is considered (see Fig. 4a). The tangential friction force and the relative sliding velocity are defined by

$$\boldsymbol{\lambda}_T = \begin{bmatrix} \lambda_{T_1} \\ \lambda_{T_2} \end{bmatrix} \quad \text{and} \quad \boldsymbol{\gamma}_T = \begin{bmatrix} \gamma_{T_1} \\ \gamma_{T_2} \end{bmatrix}. \tag{32}$$

The normal force at the contact is called λ_N. A specific force reservoir $\mathscr{C} \subset \mathbb{R}^2$ in combination with a flow rule defines the friction law at the contact. The term planar friction is used to emphasize the existence of two-dimensional friction forces in the contact plane. Other authors sometimes refer to such behavior as spatial friction (see, e.g., [5]).

3.2 Associated Coulomb friction laws

Associated Coulomb friction laws according to Definition 12 are valid for all compact and convex force

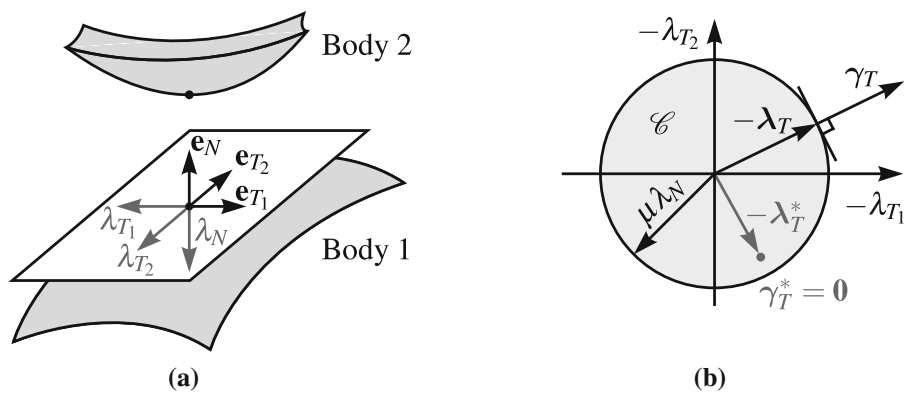

Fig. 4 **a** Contact plane and contact forces on body 1. **b** Graphical representation of isotropic friction law with stick and slip

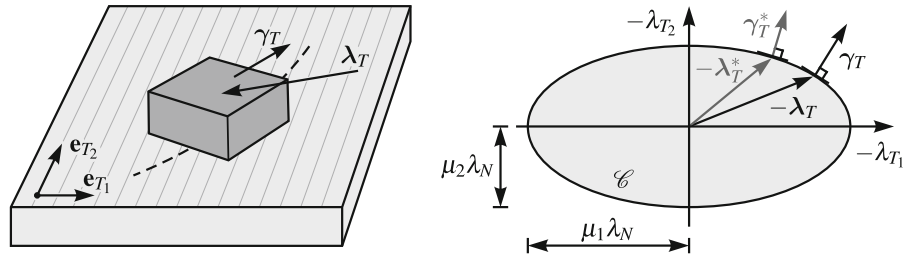

Fig. 5 **a** Body sliding on anisotropic surface. **b** Associated Coulomb friction law

reservoirs $\mathscr{C}$. The shape of the force reservoir has a great influence on the frictional behavior at a contact point. In this section, different shapes of the force reservoir are discussed.

Isotropic Friction

The constitutive behavior of stick and slip for isotropic friction in a plane is given by the following definition.

Definition 14 (*Isotropic Coulomb Friction Law*) Let $\mu > 0$ be the isotropic friction coefficient. An *isotropic Coulomb friction law* fulfills

$$\begin{aligned} &\text{(i)} \quad \boldsymbol{\gamma}_T = \mathbf{0}\,, \quad \|\boldsymbol{\lambda}_T\| \leq \mu\lambda_N, \\ &\text{(ii)} \quad \boldsymbol{\gamma}_T \neq \mathbf{0}\,, \quad -\boldsymbol{\lambda}_T = \mu\lambda_N \frac{\boldsymbol{\gamma}_T}{\|\boldsymbol{\gamma}_T\|}, \end{aligned}$$

where the fraction represents the normalized sliding velocity, i.e., the unit vector in the plane pointing in the direction of $\boldsymbol{\gamma}_T$.

This frictional behavior can be expressed with the associated Coulomb friction law (Definition 12) and a circular force reservoir $\mathscr{C}$ called Coulomb-Moreau's disk [41]:

$$\boldsymbol{\gamma}_T \in \mathscr{N}_{\mathscr{C}}(-\boldsymbol{\lambda}_T) \tag{33}$$

with $\mathscr{C} = \left\{-\boldsymbol{\lambda}_T \in \mathbb{R}^2 \mid \|\boldsymbol{\lambda}_T\| \leq \mu\lambda_N\right\}$, see Fig. 4b. For friction forces inside the force reservoir, the sliding velocity is zero. For friction forces on the boundary of the set, the vector of the sliding velocity $\boldsymbol{\gamma}_T$ is normal to the set and therefore points in the direction of $-\boldsymbol{\lambda}_T$. The magnitude of the sliding friction force is independent of the sliding direction.

Anisotropic Friction with Various Force Reservoirs

The associated Coulomb friction law is not only useful for the description of isotropic friction but can also be applied in the anisotropic case if the principle of maximum dissipation (Proposition 2) is assumed to hold. This is an assumption that is frequently made but lacks an experimental verification. In the case of anisotropic friction, the force reservoir is changed from a circle to any convex and compact shape. For symmetric force reservoirs, orthotropic force laws are obtained. For orthotropic friction, often an *ellipsoidal force reservoir* of the form

$$\mathscr{C} = \left\{-\boldsymbol{\lambda}_T \in \mathbb{R}^2 \;\middle|\; \left(\frac{-\lambda_{T_1}}{\mu_1\lambda_N}\right)^2 + \left(\frac{-\lambda_{T_2}}{\mu_2\lambda_N}\right)^2 \leq 1\right\} \tag{34}$$

is assumed. For a non-circular force reservoir, $-\boldsymbol{\lambda}_T$ and $\boldsymbol{\gamma}_T$ are generally not collinear. The force component acting orthogonal to the sliding direction causes a body sliding on a horizontal plane without the presence of external forces to deflect (see Fig. 5a, b). Only if the sliding velocity is parallel to the principal axes of the ellipsoidal force reservoir, the friction force is directly opposing it.

Orthotropic Coulomb friction during slip can also be modeled by using two independent sign functions along the principal directions of the orthotropic surface [50]. To account for the set-valued nature of Coulomb friction, the force law can be rewritten using set-valued Sign functions:

$$\begin{aligned} -\lambda_{T_1} &\in -\mu_1\lambda_N \mathrm{Sign}(\gamma_{T_1}), \\ -\lambda_{T_2} &\in -\mu_2\lambda_N \mathrm{Sign}(\gamma_{T_2}). \end{aligned} \tag{35}$$

Here, stick and slip along the two principal directions are independent of each other. A physical model exhibiting such a behavior is the X–Y table shown in Fig. 6a. Each of the two slide bearings, with friction coefficient μ_1 and μ_2, respectively, can move independently of the other. The inclusions (35) are equivalent to the associated Coulomb friction law with the *rectangular force reservoir*

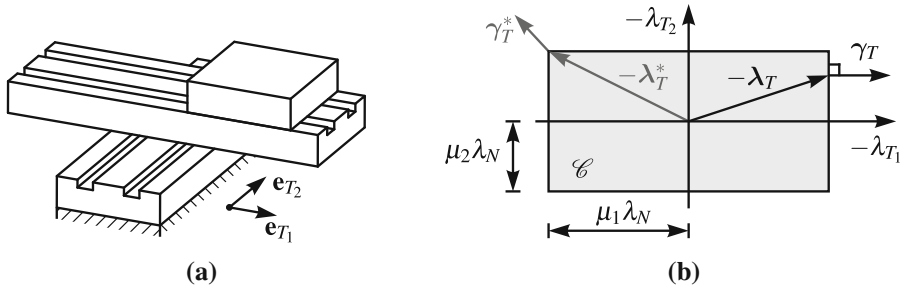

(a) **(b)**

Fig. 6 **a** Sketch of a X–Y table. **b** Graphical representation of associated Coulomb friction law with rectangular force reservoir

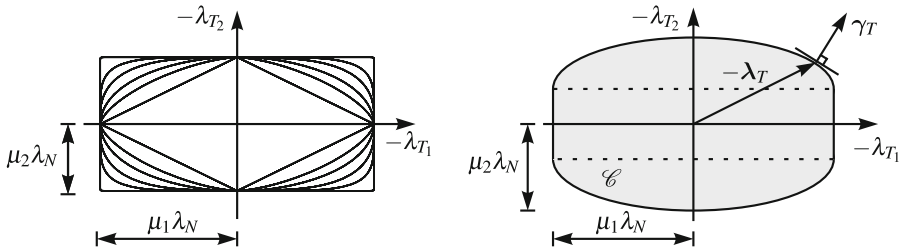

(a) **(b)**

Fig. 7 **a** Superellipsoidal friction force reservoirs with different roundness factors. **b** Friction force reservoir composed of a rectangle and two half-ellipses

$$\mathscr{C} = \left\{ -\boldsymbol{\lambda}_T \in \mathbb{R}^2 \mid \left|-\lambda_{T_1}\right| \leq \mu_1\lambda_N,\ \left|-\lambda_{T_2}\right| \leq \mu_2\lambda_N \right\}, \tag{36}$$

see Fig. 6b. The force reservoir is convex, but not strictly convex. If sliding in one of the principal directions is considered, then the slide bearing orthogonal to that direction is in the stick phase. Therefore, for a given sliding direction, a set of possible friction forces exists, namely all friction forces on the corresponding straight segment of the boundary of the force reservoir. The rate of dissipation in the case of such a convex but not strictly convex force reservoir is still unique since the component of the friction force orthogonal to the sliding velocity does not contribute to the dissipation. A unique friction force is found if the dynamics of the system is considered.

For friction forces in the corner of the rectangular force reservoir, the normal cone returns the set of all sliding directions in the corresponding quadrant. This means that for a range of sliding directions, the magnitude and direction of the friction force is the same.

Besides the elliptical and rectangular force reservoir, other convex force reservoirs for orthotropic friction are possible. A useful mathematical description of sets with two semi-axes are superellipses. The general expression for a *superellipsoidal set* with roundness factor s is given as

$$\mathscr{C} = \left\{ -\boldsymbol{\lambda}_T \in \mathbb{R}^2 \;\middle|\; \left|\frac{\lambda_{T_1}}{\mu_1\lambda_N}\right|^s + \left|\frac{\lambda_{T_2}}{\mu_2\lambda_N}\right|^s \leq 1 \right\}. \tag{37}$$

The roundness factor determines the shape of the superellipse as depicted in Fig. 7a. For $s \geq 1$ the set is convex. A rhombus is obtained for $s = 1$. The standard ellipse has a roundness factor of $s = 2$. If, in addition, $\mu_1 = \mu_2$ holds, then the force reservoir is circular and the force law reduces to the form of isotropic Coulomb friction.

The associated Coulomb friction law can be further adjusted to specific anisotropic frictional behavior by implementing suitable force reservoirs. An example of anisotropic frictional behavior is the contact of a slider on ice, as plays an important role in the numerical simulation of a bobsleigh on the surface of an ice track [51]. Without anisotropic friction, the bobsleigh would be unable to steer. In [31], it is assumed that the force reservoir consists of two half-ellipses connected to a rectangle, see Fig. 7b.

Capability and Limitations of the Friction Law

The formulation of the friction force law as normal cone on the friction force reservoir $\mathscr{C}$ is an effective method to describe the set-valued nature of stick and slip. By adjusting the shape of the force reservoir, the

magnitude of the friction force for different sliding directions is specified and the relationship between the sliding direction and the direction of the friction force follows from normality to the set. In order to guarantee dissipativity of the friction law, the force reservoir necessarily has to contain the origin. The formulation is capable of describing many aspects of anisotropic frictional behavior. However, all chosen friction force reservoirs have to fulfill the condition of being convex. Non-convex sets are not allowed, since the definition of normal cone inclusions (see Definition 6) is only valid for convex sets. This limitation makes it impossible to incorporate more complex non-convex force reservoirs that are discussed later in this work.

3.3 Non-associated anisotropic friction laws

The assumption of maximum dissipation which holds for the associated Coulomb friction law is not necessarily valid for real anisotropic frictional behavior. In this section, other possible anisotropic friction laws are briefly discussed. Since the sliding direction in those cases is not directly related to the shape of the force reservoir, the force laws are called non-associated force laws.

Collinear Friction Law

The associated Coulomb friction law described above has for non-circular force reservoirs, a limited number of sliding directions where the friction force directly opposes the direction of sliding. A specific anisotropic friction law which is often encountered in the literature (e.g., [52]) is based on friction forces that always directly oppose the sliding direction. In this work, such a friction law is called collinear friction law.

Definition 15 (*Collinear Friction Law*) A *collinear friction law* is characterized by a friction force during slip that is always parallel to the sliding direction and opposes the relative sliding velocity.

The friction coefficient and with that, the magnitude of the friction force is dependent on the sliding direction. During slip, the force law can be expressed in the form

$$\boldsymbol{\gamma}_T \neq \mathbf{0}\,; \quad -\boldsymbol{\lambda}_T = \mu(\boldsymbol{\gamma}_T)\lambda_N \frac{\boldsymbol{\gamma}_T}{\|\boldsymbol{\gamma}_T\|}, \tag{38}$$

where the scalar magnitude of the friction force is multiplied by the normalized vector of the relative sliding velocity. As before, the shape of the force reservoir has to be defined. In the following, an ellipsoidal shape as given in Eq. (34) is assumed. The friction coefficients along the major axes are μ_1 and μ_2. With the diagonal matrix

$$\boldsymbol{T} = \begin{bmatrix} \frac{1}{\mu_1 \lambda_N} & 0 \\ 0 & \frac{1}{\mu_2 \lambda_N} \end{bmatrix} \tag{39}$$

the force reservoir $\mathscr{C}$ can be expressed as

$$\mathscr{C} = \left\{ -\boldsymbol{\lambda}_T \in \mathbb{R}^2 \;\middle|\; \sqrt{\boldsymbol{\lambda}_T^{\mathrm{T}} \boldsymbol{T}^2 \boldsymbol{\lambda}_T} \leq 1 \right\}. \tag{40}$$

The sliding friction force is then given by

$$-\boldsymbol{\lambda}_T = \frac{1}{\sqrt{\boldsymbol{\gamma}_T^{\mathrm{T}} \boldsymbol{T}^2 \boldsymbol{\gamma}_T}} \boldsymbol{\gamma}_T, \tag{41}$$

i.e., the friction coefficient as a function of the sliding direction is

$$\mu(\boldsymbol{\gamma}_T) = \frac{1}{\sqrt{\boldsymbol{\gamma}_T^{\mathrm{T}} \boldsymbol{T}^2 \boldsymbol{\gamma}_T}} \frac{\|\boldsymbol{\gamma}_T\|}{\lambda_N} = \frac{\sqrt{\gamma_{T_1}^2 + \gamma_{T_2}^2}}{\sqrt{\left(\frac{\gamma_{T_1}}{\mu_1}\right)^2 + \left(\frac{\gamma_{T_2}}{\mu_2}\right)^2}}. \tag{42}$$

The force law can be transformed into a set-valued normal cone inclusion force law by making use of the transformation property Eq. (9). Considering the fact that under the linear mapping $\boldsymbol{T}$ the collinear vectors $-\boldsymbol{\lambda}_T$ and $\boldsymbol{\gamma}_T$ remain collinear, the force law can be illustrated by the graph shown in Fig. 8a. The transformation matrix $\boldsymbol{T}$ is chosen such that the elliptical set $\mathscr{C}$ is transformed to the circular set $\boldsymbol{T}\mathscr{C}$ with radius one and the force law is therefore represented by the inclusion

$$\boldsymbol{T}\boldsymbol{\gamma}_T \in \mathscr{N}_{\boldsymbol{T}\mathscr{C}}(-\boldsymbol{T}\boldsymbol{\lambda}_T). \tag{43}$$

This inclusion can be transformed to a normal cone inclusion on the ellipsoidal force reservoir $\mathscr{C}$ using Eq. (9),

$$\boldsymbol{T}^2\boldsymbol{\gamma}_T \in \mathscr{N}_{\mathscr{C}}(-\boldsymbol{\lambda}_T). \tag{44}$$

Figure 8b shows a graphical representation of this collinear force law with ellipsoidal force reservoir. Since the friction force is directly opposing the sliding velocity, a sliding body experiencing such a force law

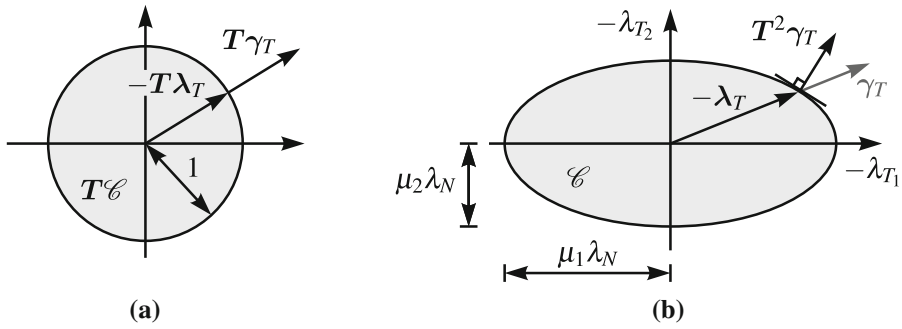

Fig. 8 **a** Collinear friction law transformed to circle. **b** Collinear friction law with elliptical force reservoir

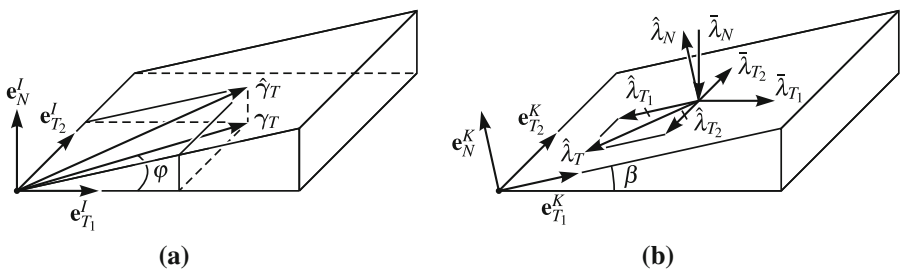

Fig. 9 **a** Relative sliding velocity of a spring in contact with an inclined plane. **b** Contact forces acting on a spring and the inclined plane depicted in local and global reference frame. Adapted from [25]

is not deflected. Writing the force law as normal cone inclusion allows for an efficient numerical treatment of the set-valued nature of Coulomb friction.

Asperity Model

Microscopic surface asperities play an important role in the frictional behavior of contacting bodies. Randomly distributed asperities result in isotropic friction. Anisotropic friction can be modeled by the superposition of a random distribution and a systematical order of asperities. In [24], such a model is introduced to describe anisotropic friction on machined metal surfaces. The macroscopic frictional behavior is determined by investigating the behavior of a mass sliding on an isotropic inclined plane. Sliding along the plane on a fixed level curve leads to a macroscopic friction force equal to the force induced by the isotropic friction of the mass on the plane. However, pushing the mass up the inclined plane requires a higher force which leads to anisotropic macroscopic behavior. The combination of inclined planes to parallel wedge-shaped asperities results in a model capable of specifying the friction force for all sliding directions. In general, the model results in non-convex force reservoirs. The relationship between the friction force and the sliding direction is not defined by normality of the sliding direction to the force reservoir $\mathscr{C}$, but by normality to a different convex direction set $\mathscr{D}$. The model therefore leads to a non-associated friction law.

In a more advanced model [25], one of the contacting surfaces is still modeled with parallel wedge-shaped asperities. The second surface, however, now consists of uniformly distributed springs with uniform stiffness attached to a moving plane. Contact compliance in normal and tangential direction is neglected. The springs are used to model the friction force when the two surfaces move parallel to each other with a constant distance. Figure 10a shows an example of a fixed wedge-shaped asperity with the same inclination angle β on both sides in contact with a moving plate with spring asperities. No separation of the springs and the wedge asperities is assumed and the springs are always compressed. Following the calculations of [25], the set of admissible macroscopic friction forces acting in the contact plane can be obtained. The macroscopic relative sliding velocity is $\boldsymbol{\gamma}_T$. We denote the relative sliding velocity of a single spring in contact with an inclined plane by $\hat{\boldsymbol{\gamma}}_T$ as shown in Fig. 9a. The projection of $\hat{\boldsymbol{\gamma}}_T$ on the macroscopic contact plane is $\boldsymbol{\gamma}_T$, being under the angle φ to the $\mathbf{e}_{T_1}^I$-axis. The contact forces acting on a single spring and an inclined plane are depicted in Fig. 9b. Along the inclined $\mathbf{e}_{T_1}^K$-$\mathbf{e}_{T_2}^K$-plane, isotropic friction with friction coefficient μ is present. The magnitude $\hat{\lambda}_T$ of the friction force acting on the spring is therefore given by $\hat{\lambda}_T = \mu\hat{\lambda}_N$, where $\hat{\lambda}_N$ represents the normal force, orthogonal to the inclined plane. The contact forces expressed in the K-frame acting on the spring are in equilibrium with

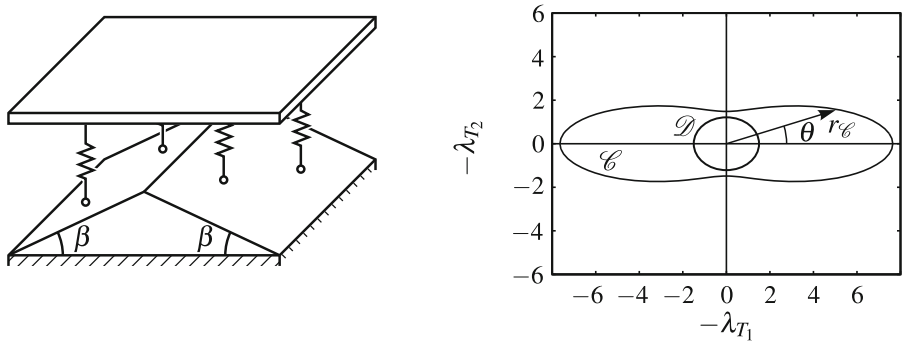

Fig. 10 **a** Asperity model with wedge-shaped asperities in contact with springs. **b** Resulting non-convex force reservoir

(a) **(b)**

the contact forces acting on the inclined plane $\bar{\lambda}_{T_1}, \bar{\lambda}_{T_2}$ and $\bar{\lambda}_N$ expressed in the I-frame of the macroscopic contact plane. It holds that

$$\bar{\lambda}_N = \hat{\lambda}_N \cos\beta - \hat{\lambda}_{T_1} \sin\beta, \tag{45}$$

$$\bar{\lambda}_{T_1} = \hat{\lambda}_N \sin\beta + \hat{\lambda}_{T_1} \cos\beta, \tag{46}$$

$$\bar{\lambda}_{T_2} = \hat{\lambda}_{T_2}. \tag{47}$$

The maximum friction force in $\mathbf{e}^K_{T_1}$-direction is $\hat{\lambda}_{T_1} = \mu\hat{\lambda}_N$. Substitution of the friction force in Eq. (45) yields

$$\bar{\lambda}_N = \hat{\lambda}_N \left(\cos\beta - \mu \sin\beta\right). \tag{48}$$

With the conditions $\hat{\lambda}_N > 0$ and $\bar{\lambda}_N > 0$, the admissible range of the friction coefficient is obtained as $\mu < \cot(\beta)$. From Eqs. (45)–(47), functions describing the macroscopic friction forces of a single spring can be calculated in the form $\bar{\lambda}_{T_1} = \bar{\lambda}_N H_{T_1}(\mu, \beta, \varphi)$ and $\bar{\lambda}_{T_2} = \bar{\lambda}_N H_{T_2}(\mu, \beta, \varphi)$, where H_{T_1} and H_{T_2} are functions of μ, β and φ, see [25]. The vertical force $\bar{\lambda}_N$ depends on the displacement of the corresponding spring. If a set of springs in contact with both sides of parallel wedge-shaped asperities with the same inclination angle β on both sides is considered, then the macroscopic friction forces are found as

$$\begin{aligned} \lambda_{T_1} &= \frac{\lambda_N}{2}\left(H_{T_1}(\mu, \beta, \varphi) + H_{T_1}(\mu, -\beta, \varphi)\right), \\ \lambda_{T_2} &= \frac{\lambda_N}{2}\left(H_{T_2}(\mu, \beta, \varphi) + H_{T_2}(\mu, -\beta, \varphi)\right). \end{aligned} \tag{49}$$

Here, the macroscopic normal force λ_N is a function of the spring stiffness and the constant mean spring displacement. Equation (49) describes the friction forces for all possible sliding directions and allow for the calculation of the set of admissible macroscopic friction forces acting in the contact plane. The force reservoir can be expressed in polar coordinates by

$$r_{\mathscr{C}}(\theta) = \frac{\mu\lambda_N}{\cos\beta} \frac{\sqrt{\cos^2\beta\cos^2\theta + \sin^2\theta}}{\sin^2\theta + \left[1 - \left(1+\mu^2\right)\sin^2\beta\right]\cos^2\theta}, \tag{50}$$

where θ describes the angle between the $\mathbf{e}^I_{T_1}$-axis and the direction of the friction force (see [25]). The inclination angle lies in the range $0° \leq \beta < 90°$. For $\beta = 0°$, the isotropic friction law with circular force reservoir is recovered. In Fig. 10b, the force reservoir $\mathscr{C}$ is shown for the parameters $\mu = 1.2$ and $\beta = 36°$. For the given parameters, the set is clearly non-convex. However, the set $\mathscr{C}$ is always star-shaped since $r_{\mathscr{C}}(\theta) > 0$ for all θ, if admissible values of μ and β are considered in Eq. (50).

The sliding direction is not associated with the friction force reservoir. Instead, it is defined by normality to an ellipsoidal direction set $\mathscr{D}$ at the intersection of the boundary of the set and the direction of the negative friction force $-\boldsymbol{\lambda}_T$. The ellipsoidal set is given by

$$\mathscr{D} = \left\{ -\boldsymbol{\lambda}_T \in \mathbb{R}^2 \;\middle|\; \left(\frac{-\lambda_{T_1}}{p_1}\right)^2 + \left(\frac{-\lambda_{T_2}}{p_2}\right)^2 \leq 1 \right\}, \tag{51}$$

with the semi-axes ratio

$$\frac{p_2}{p_1} = \cos\beta. \tag{52}$$

For the parameters given above, the set is also shown in Fig. 10b. The scaling of the direction set $\mathscr{D}$ is irrelevant and can be chosen arbitrarily.

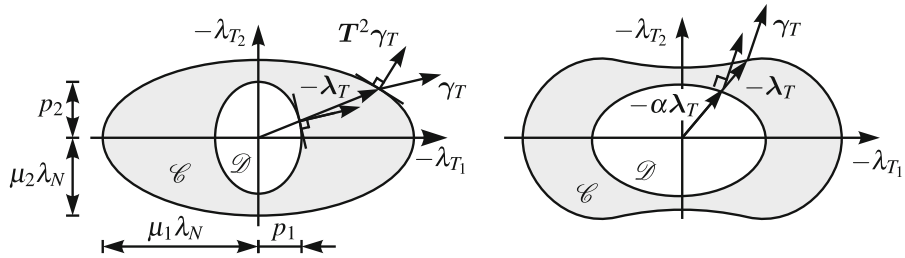

Fig. 11 Graphical representation of non-associated friction law **a** with ellipsoidal sets **b** with non-convex force reservoir

In the literature, the non-convexity of the force reservoir is sometimes neglected and the two sets $\mathscr{C}$ and $\mathscr{D}$ are assumed to both be of ellipsoidal or superellipsoidal shape with the same roundness factor [25,53,54]. A graphical representation of the friction law for ellipsoidal sets is shown in Fig. 11a. Similar to Sect. 3.3, the force law in that case can be formulated as normal cone inclusion. Here, the transformation matrix $\boldsymbol{T}$ is given by

$$\boldsymbol{T} = \begin{bmatrix} \frac{p_1}{\mu_1 \lambda_N} & 0 \\ 0 & \frac{p_2}{\mu_2 \lambda_N} \end{bmatrix} \tag{53}$$

and the force law is written as

$$\boldsymbol{T}^s \boldsymbol{\gamma}_T \in \mathscr{N}_{\mathscr{C}}(-\boldsymbol{\lambda}_T), \tag{54}$$

where s represents the roundness factor of the superellipsoidal sets. The collinear friction law with ellipsoidal force reservoir ($s = 2$) is contained in that formulation and is obtained for a circular set $\mathscr{D}$ for which Eq. (53) and (54) equal Eqs. (39) and (44), respectively. If the set $\mathscr{D}$ is taken equal to the force reservoir $\mathscr{C}$, then the associated Coulomb friction law (Definition 12) is recovered.

To analyze the existence of a convex pseudo-potential, the force law has to be checked for cyclic maximal monotonicity [8]. From Proposition 3 it follows that the force law is not maximal monotone and consequently not cyclically maximal monotone if $\mathscr{C}$ and $\mathscr{D}$ differ in shape. Thus, in general, no convex pseudo-potential exists. Instead, following [26,54,55], a bipotential can be found. A force law capable of handling non-convex force reservoirs is derived in the following section.

3.4 Extended normal cone inclusion friction law

The asperity model motivated by [25] and described in Sect. 3.3 as well as the tensor formulation of anisotropic friction by [56] both result in non-associated friction force laws with possibly non-convex force reservoirs. The force law Eq. (54), however, is only valid for convex force reservoirs. In this section a set-valued force law allowing for different shapes of the force reservoir $\mathscr{C}$ and the direction set $\mathscr{D}$ as well as for non-convex force reservoirs is developed in the framework of convex analysis.

Definition 16 (Extended Normal Cone Inclusion Friction Law) Let $\mathscr{C} \subset \mathbb{R}^2$ be a compact and star-shaped set and let $\mathscr{D} \subset \mathbb{R}^2$ be a compact and convex set with $\mathscr{D} \subseteq \mathscr{C}$ and $\mathbf{0} \in \operatorname{int} \mathscr{D}$. The gauge functions of the sets are given by $k_{\mathscr{C}}$ and $k_{\mathscr{D}}$. A Coulomb-type friction law is called an *extended normal cone inclusion friction law* if

$$\boldsymbol{\gamma}_T \in \mathscr{N}_{\mathscr{D}}(-\alpha \boldsymbol{\lambda}_T) \tag{55}$$

with

$$\alpha = \frac{1}{k_{\mathscr{D}}(-\boldsymbol{\lambda}_T) - k_{\mathscr{C}}(-\boldsymbol{\lambda}_T) + 1}. \tag{56}$$

A graphical representation of such a friction law is shown in Fig. 11b. The nonempty sets $\mathscr{C}$ and $\mathscr{D}$ can be represented as the level sets of their gauge functions $k_{\mathscr{C}}$ and $k_{\mathscr{D}}$ by

$$\mathscr{C} = \{-\boldsymbol{\lambda}_T \mid k_{\mathscr{C}}(-\boldsymbol{\lambda}_T) \leq 1\}, \tag{57}$$

$$\mathscr{D} = \{-\boldsymbol{\lambda}_T \mid k_{\mathscr{D}}(-\boldsymbol{\lambda}_T) \leq 1\}. \tag{58}$$

The origin is required to be contained in the interior of $\mathscr{D}$ to guarantee that $k_{\mathscr{D}}(-\boldsymbol{\lambda}_T)$ is defined for all friction forces. The sliding direction is given by normality to

the direction set $\mathscr{D}$. Instead of formulating a force law as normal cone inclusion on the force reservoir as in Eq. (54), a normal cone inclusion on set $\mathscr{D}$ is defined. Here, the normality condition is directly fulfilled and non-convex force reservoirs are no longer excluded. The challenge is the accurate description of the stick phase since the force reservoir is independent of $\mathscr{D}$ and the condition $\boldsymbol{\gamma}_T = \mathbf{0}$ for friction forces inside the force reservoir is not automatically fulfilled.

a) $-\boldsymbol{\lambda}_T \in \operatorname{int} \mathscr{C}$: For all friction forces in the interior of the force reservoir, the sliding velocity must be zero. Since gauge functions return values less than one for points in the interior of the corresponding set, it must hold that $\boldsymbol{\gamma}_T = \mathbf{0}$ for $k_{\mathscr{C}}(-\boldsymbol{\lambda}_T) < 1$.

b) $-\boldsymbol{\lambda}_T \in \operatorname{bdry} \mathscr{C}$: For friction forces at the boundary of the force reservoir, the sliding velocity is defined by the normal cone to the set $\mathscr{D}$ at the point of the friction force scaled to the boundary of $\mathscr{D}$ by the parameter α, i.e.,

$$\boldsymbol{\gamma}_T \in \mathscr{N}_{\mathscr{D}}(-\alpha\boldsymbol{\lambda}_T) \quad \text{with} \quad -\alpha\boldsymbol{\lambda}_T \in \operatorname{bdry} \mathscr{D}. \tag{59}$$

With the gauge function being one for points at the boundary of the set, Eq. (59) can be rewritten as:

$$\boldsymbol{\gamma}_T \in \mathscr{N}_{\mathscr{D}}(-\alpha\boldsymbol{\lambda}_T) \quad \text{for} \quad k_{\mathscr{C}}(-\boldsymbol{\lambda}_T) = 1 \tag{60}$$

with $k_{\mathscr{D}}(-\alpha\boldsymbol{\lambda}_T) = 1$. The scaling function $\alpha = f(-\boldsymbol{\lambda}_T)$ thereby scales the friction force to the interior of $\mathscr{D}$ if the friction force lies in the interior of the force reservoir and to the boundary of $\mathscr{D}$ if the force is at the boundary of $\mathscr{C}$. It is therefore designed as

$$\alpha : \begin{cases} < \frac{1}{k_{\mathscr{D}}(-\boldsymbol{\lambda}_T)} & \text{for} \quad k_{\mathscr{C}}(-\boldsymbol{\lambda}_T) < 1 \\ = \frac{1}{k_{\mathscr{D}}(-\boldsymbol{\lambda}_T)} & \text{for} \quad k_{\mathscr{C}}(-\boldsymbol{\lambda}_T) = 1. \end{cases} \tag{61}$$

These conditions are combined in the function

$$\alpha = \frac{1}{k_{\mathscr{D}}(-\boldsymbol{\lambda}_T) - k_{\mathscr{C}}(-\boldsymbol{\lambda}_T) + 1}, \tag{62}$$

where the argument of the scaling function $\alpha(-\boldsymbol{\lambda}_T)$ is omitted for brevity. To ensure that the scaling function α is always positive, the condition

$$k_{\mathscr{D}}(-\boldsymbol{\lambda}_T) \geq k_{\mathscr{C}}(-\boldsymbol{\lambda}_T) \tag{63}$$

is imposed. Therefore, $\mathscr{D} \subseteq \mathscr{C}$ must apply. This can be reached for all star-shaped $\mathscr{C}$ with $\mathbf{0} \in \operatorname{int} \mathscr{C}$ since it is always possible to scale the compact set $\mathscr{D}$ without loss of generality.

One of the advantages of the described force law as normal cone inclusion on the set $\mathscr{D}$ is that the force reservoir is no longer restricted to convex shapes. The definitions of gauge functions and corresponding level sets Eq. (58) are also valid for sets that are star-shaped with respect to the origin [43]. Star-shaped sets are possibly non-convex. Limiting the force reservoir $\mathscr{C}$ to star-shaped and the set $\mathscr{D}$ to convex shapes ensures that for a given $\boldsymbol{\gamma}_T$ and known dynamics of a system, a unique friction force $\boldsymbol{\lambda}_T$ is assigned. For star-shaped force reservoirs, the magnitude of a friction force acting in a certain direction during slip is well defined. During stick the friction force in that direction can take any value between the value of the sliding friction force and zero.

If the direction set $\mathscr{D}$ is even strictly convex, then a given nonzero relative sliding velocity $\boldsymbol{\gamma}_T$ is in the normal cone of the compact set $\mathscr{D}$ at a unique boundary point $z = -\alpha(-\boldsymbol{\lambda}_T)\boldsymbol{\lambda}_T$ (see Fig. 11). From the scaled friction force z, the friction force $-\boldsymbol{\lambda}_T$ can be calculated by expressing the scaling parameter α as a function of z, i.e.,

$$-\boldsymbol{\lambda}_T = \frac{1}{\alpha} z, \tag{64}$$

$$= (k_{\mathscr{D}}(-\boldsymbol{\lambda}_T) - k_{\mathscr{C}}(-\boldsymbol{\lambda}_T) + 1) z. \tag{65}$$

$$= \frac{1}{\alpha}(k_{\mathscr{D}}(z) - k_{\mathscr{C}}(z) + \alpha) z. \tag{66}$$

Herein, α from Eq. (62) is substituted, then the arguments of the gauge function are replaced with Eq. (64) and the fact that the gauge functions are positively homogeneous of degree one is used. If again Eq. (64) is substituted in Eq. (66), the expression

$$\alpha(z) = k_{\mathscr{C}}(z) - k_{\mathscr{D}}(z) + 1 \tag{67}$$

is obtained, which together with Eq. (64) allows for the calculation of the friction force for known values of z. For z on the boundary of $\mathscr{D}$, the gauge function $k_{\mathscr{D}}(z)$ is equal to one.

In analogy to Proposition 1, in which the dissipativity of the associated friction law is proven, we discuss the dissipativity of the extended normal cone inclusion friction law.

Proposition 5 *(Dissipativity of Extended Normal Cone Inclusion Friction Law) The extended normal cone inclusion friction law is strictly dissipative.*

Proof Rewriting the normal cone inclusion with the subdifferential of the indicator function and again using the Fenchel equality results in

$$\begin{aligned} \boldsymbol{\gamma}_T \in \partial \Psi_{\mathscr{D}}(-\alpha \boldsymbol{\lambda}_T) &\iff -\alpha \boldsymbol{\lambda}_T \in \partial \Psi^*_{\mathscr{D}}(\boldsymbol{\gamma}_T) \\ &\iff -\alpha \boldsymbol{\lambda}_T^{\mathrm{T}} \boldsymbol{\gamma}_T = \Psi_{\mathscr{D}}(-\alpha \boldsymbol{\lambda}_T) + \Psi^*_{\mathscr{D}}(\boldsymbol{\gamma}_T). \end{aligned} \tag{68}$$

The indicator function $\Psi_{\mathscr{D}}(-\alpha \boldsymbol{\lambda}_T)$ is zero because the scaled friction force is always in the set $\mathscr{D}$. It holds that $\Psi^*_{\mathscr{D}}(\boldsymbol{\gamma}_T) > 0$ for all $\boldsymbol{\gamma}_T \neq \mathbf{0}$ since $\mathbf{0} \in \operatorname{int} \mathscr{D}$. Therefore, using $\alpha > 0$, the dissipation rate for the extended friction force law is given as

$$D(-\boldsymbol{\lambda}_T, \boldsymbol{\gamma}_T) = -\boldsymbol{\lambda}_T^{\mathrm{T}} \boldsymbol{\gamma}_T = \frac{1}{\alpha} \Psi^*_{\mathscr{D}}(\boldsymbol{\gamma}_T) > 0. \qquad \square$$

Implementation in a Time-Stepping Method

As described in Sect. 2.3, set-valued force laws given in the form of normal cone inclusions can be used for the numerical simulation of nonsmooth systems by rewriting them as implicit proximal point functions. In order to implement the extended normal cone inclusion friction law in the iteration scheme, Eq. (22) has to be replaced by

$$\boldsymbol{P}_T^{k+1} = -\frac{1}{\alpha^k} \operatorname{prox}_{\mathscr{D}}(-\alpha^k \boldsymbol{P}_T^k + r \boldsymbol{\gamma}_{T\mathrm{E}}^k), \quad r > 0, \tag{69}$$

where the scaling parameter is determined by

$$\alpha^k = \frac{1}{k_{\mathscr{D}}(-\boldsymbol{P}_T^k) - k_{\mathscr{C}}(-\boldsymbol{P}_T^k) + 1} \tag{70}$$

in each iteration [57].

Capability and Limitations of the Friction Law

The associated force law, based on normality of the sliding direction to the friction force reservoir $\mathscr{C}$, is limited to convex shapes of the force reservoir. The extended normal cone inclusion force law does not have this limitation. It allows for the implementation of non-convex but star-shaped force reservoirs, which is motivated, e.g., by the tensor formulation described by [28] and the asperity model (see Sect. 3.3). Non-convex and not star-shaped force reservoirs are not permitted since gauge functions are not defined for such sets. However, force reservoirs that are not star-shaped are not allowed for dry friction laws since for such sets a decrease in the static friction force may lead to a stick-slip transition. While the force reservoir may be non-convex, the direction set $\mathscr{D}$ in this work is limited to convex sets.

The formulation of the force law as normal cone inclusion makes it possible to represent the set-valued nature of friction with the transition of stick and slip. Thereby, the advantage of the associated Coulomb friction law is retained. The extended friction law reduces to the associated Coulomb friction law if both sets are convex and $\mathscr{C} = a\mathscr{D}$ for some $a \in \mathbb{R}^+$ which can be taken equal to one, i.e., $\mathscr{C} = \mathscr{D}$. Collinear force laws are given for a circular shape of the direction set $\mathscr{D}$. Unlike in Sect. 3.3, where only ellipsoidal force reservoirs are considered for the collinear force law, here, the shape of the force reservoir is arbitrary as long as it is star-shaped. If both sets have a circular shape, then the isotropic Coulomb friction force law is recovered.

In the following, the force laws given in tensor formulation by [28] are considered as examples. Figure 12 shows the graphical representation of a number of non-associated force laws. In this work, the direction sets $\mathscr{D}$ are added. The sets are determined numerically under the condition of normality of the sliding direction to the boundary of the set $\mathscr{D}$. The method is similar to the processing of the experimental data which is described in more detail in Sect. 5.2. The boundary of $\mathscr{D}$ is described in polar coordinates by

$$r_{\mathscr{D}}(\theta) = r_{\mathscr{D}}(0) \mathrm{e}^{\int_0^\theta \tan(\tilde{\theta} - \varphi) \mathrm{d}\tilde{\theta}}, \tag{71}$$

where θ is the angle between the friction force and a fixed axis and φ is the angle between the sliding direction and the same axis (see Fig. 12**c**). The initial value $r_{\mathscr{D}}(0)$ is chosen such that $\mathscr{D} \subseteq \mathscr{C}$.

Figure 12a shows an orthotropic force law with ellipsoidal force reservoir. The set $\mathscr{D}$ is also an ellipse with the same orientation of the major axes but with a different semi-axes ratio which causes the non-associativity of the force law. The force laws shown in Fig. 12b, c also allow for a direct calculation of a closed convex set $\mathscr{D}$. In the case of the force law with nonconstant friction tensor shown in Fig. 12b, the set $\mathscr{D}$ is a circle which corresponds to a collinear force law.

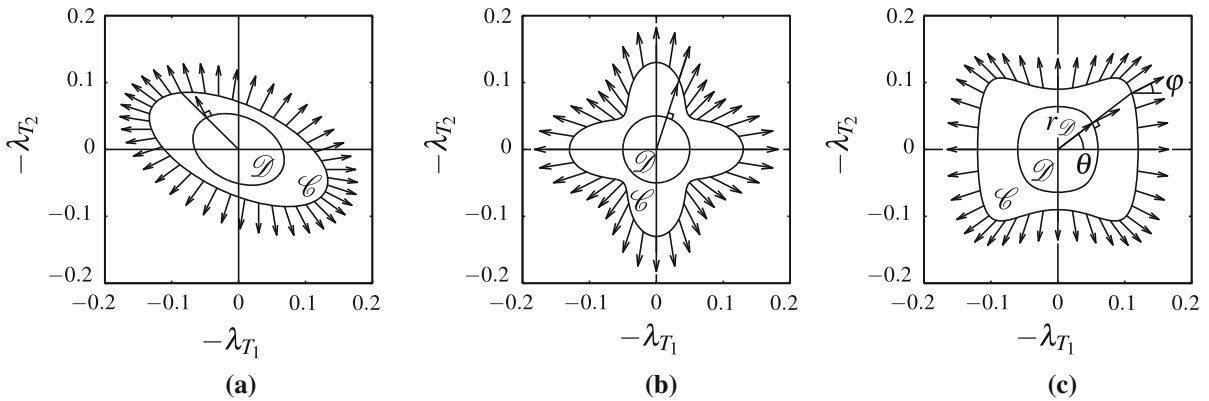

Fig. 12 Graphical representation of non-associated anisotropic friction force laws with parameters from [56] and calculated direction sets $\mathscr{D}$. **a** Orthotropic force law. **b** Force law with nonconstant friction tensor. **c** Force law with fourth order tensor

4 Friction-induced instability

This section is concerned with stability properties of mechanical systems with friction. Despite the fact that many researchers have extensively studied friction-induced vibrations, the underlying mechanisms are still not fully understood. Especially, the influence of anisotropic friction on the stability of a sliding motion has not been studied yet. In this work, systems with a single frictional contact point are considered. First, different isotropic friction-induced instability phenomena are classified according to their underlying mechanisms. In Sect. 4.2, anisotropic friction is shown to be a possible cause of self-excited vibrations that previously has been ignored by the research community.

4.1 Classification of isotropic friction-induced instability phenomena

A n-DOF mechanical system with generalized positions $\boldsymbol{q} \in \mathbb{R}^n$ and velocities $\boldsymbol{u} = \dot{\boldsymbol{q}} \in \mathbb{R}^n$ and a single frictional contact point is described by the equation of motion

$$\boldsymbol{M}\dot{\boldsymbol{u}} - \boldsymbol{h}(\boldsymbol{q}, \boldsymbol{u}) = \boldsymbol{w}_N \lambda_N + \boldsymbol{W}_T \boldsymbol{\lambda}_T, \tag{72}$$

a friction law $-\boldsymbol{\lambda}_T \in \mathscr{F}(\boldsymbol{\gamma}_T, \lambda_N)$ and a unilateral constraint $g_N(\boldsymbol{q}) \geq 0$. The generalized force directions in normal and tangential direction are denoted by $\boldsymbol{w}_N \in \mathbb{R}^n$ and $\boldsymbol{W}_T \in \mathbb{R}^{n \times p}$. For the relative sliding velocity $\boldsymbol{\gamma}_T \in \mathbb{R}^p$ it holds that

$$\boldsymbol{\gamma}_T = \boldsymbol{W}_T^{\mathrm{T}} \boldsymbol{u} - \boldsymbol{\chi}, \tag{73}$$

where $\boldsymbol{\chi} \in \mathbb{R}^p$ represents a tangential velocity at the contact point, e.g., originating from the movement of a belt. We assume that there is no explicit time dependence of the normal contact distance and the relative sliding velocity ($\boldsymbol{\chi} = \text{const.}$).

In Fig. 13 isotropic friction-induced instability phenomena are summarized. The three underlying mechanisms of instability are (a) a nonconstant friction coefficient causing stick-slip vibrations, (b+c) a nonconstant normal force leading to geometrically induced instability and (d) a follower force behavior of the friction force. In all cases, the friction force during forward slip is given by an isotropic friction law. Two of the parameters: friction coefficient, normal force and generalized force direction are held constant in each case, while the third is given as a function of the generalized coordinates or velocities.

The archetype model of friction-induced vibrations is the one degree of freedom oscillator in contact with a moving surface often referred to as block-on-belt model (see Fig. 13a). The stick-slip behavior of the model is extensively studied in the literature, e.g., by [59–61]. The key aspect is that the friction coefficient is assumed to be a function of the magnitude of the sliding velocity. A decreasing friction coefficient for an increasing sliding velocity, known as Stribeck effect, causes a negative damping coefficient in the linearized equation of motion, which leads to Hopf-type instability of the equilibrium of the system.

For Coulomb friction, the magnitude of the friction force is not only dependent on the friction coefficient

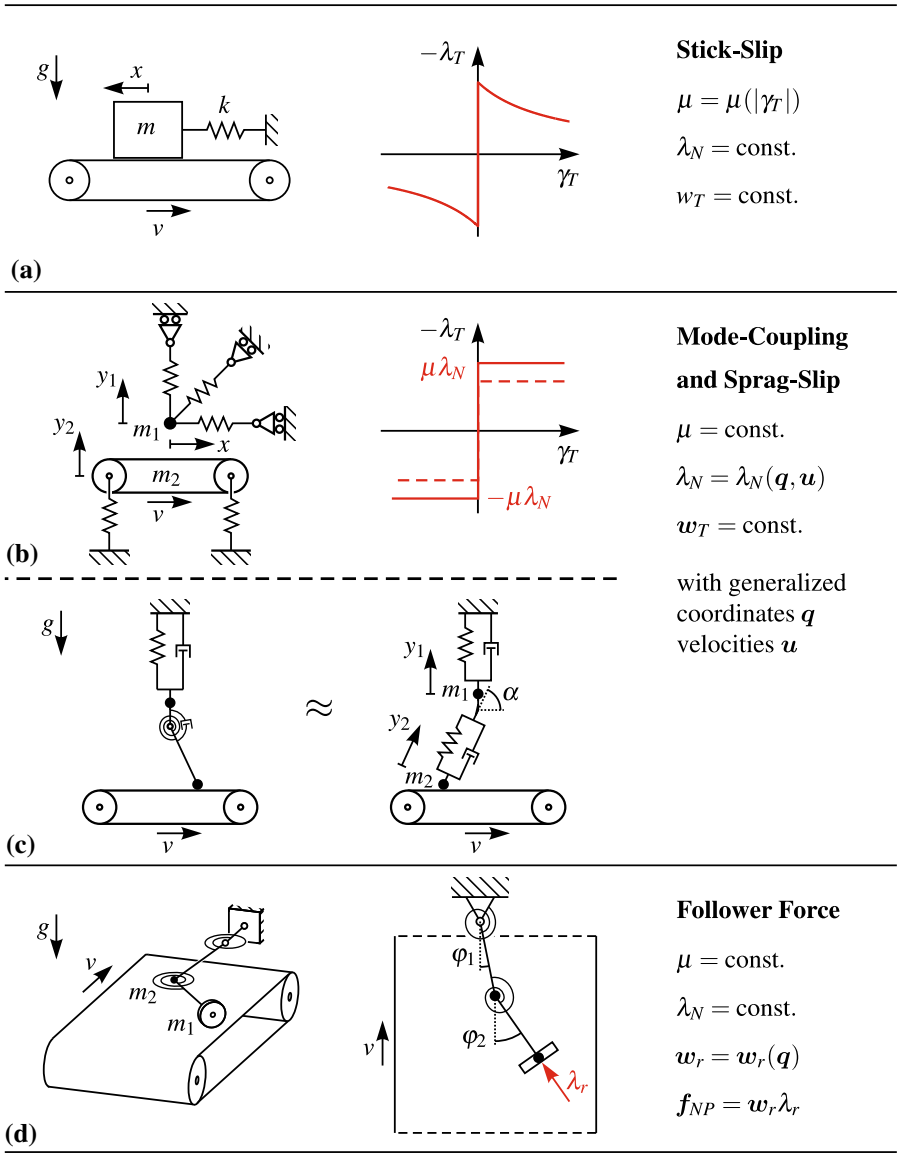

Fig. 13 Isotropic friction-induced instability phenomena. **a** Stick-slip oscillator and Stribeck friction characteristic. **b** Mechanical model to illustrate mode-coupling. **c** Frictional impact oscillator and simplified model (adapted from [58]). **d** Mechanical model of a system with frictional follower force

μ, but also on the normal force λ_N. Depending on the geometry of a mechanical system, the normal force may be a function of the generalized coordinates or velocities of the system. Such a dependence of the normal force is responsible for two instability phenomena that occur for isotropic friction without Stribeck effect. Mode-coupling instability is characterized by the convergence of oscillation frequencies of structural modes under the influence of a parameter. When they merge, a pair of an unstable and stable mode is created [35].

In Fig. 13b a planar three degree of freedom model is proposed. It consists of a mass being constrained by springs that are always horizontal, vertical or diagonal, respectively, and a belt attached to the ground via vertical springs. The belt is constrained to move only in the vertical direction. Small vibrations are considered, i.e., geometric nonlinearity due to the springs is neglected. The model differs from the models presented by [62] and [63] in that the mass is in direct contact with the belt, instead of the contact between a massless slider and the belt. If the system with closed

contact is considered, in addition to the symmetric structural coupling terms, displacement dependent frictional coupling terms occur in the equation of motion that can cause instability of the equilibrium. Besides mode-coupling, sprag-slip is a friction-induced instability phenomenon occurring due to a nonconstant normal force. This effect has first been described in the context of brake squeal in [34] using a system of inclined rigid rods pressed on a moving surface. In [64], an elastic beam in contact with a belt is used to model sprag-slip, while [58] made use of the multibody system shown in Fig. 13c to model a similar effect, which is closely related to the Painlevé paradox [65]. The frictional impact oscillator, consisting of a rigid rod, two pointmasses and linear as well as rotational springs and dampers, can be approximated for small angles with linear springs and dampers as shown in the same Fig. [58]. Unlike in the example of mode-coupling, where the dependence of the normal force on the displacement is responsible for the instability of an equilibrium, in this case the feedback of the velocity dependent part of the normal force causes the equilibrium to become unstable.

If the friction coefficient as well as the normal force are assumed to be constant, the follower force characteristic of a friction force can be a third cause of friction-induced instability. Such a force is acting on a body and changing the direction according to the displacement of the body. Frictional follower forces occur, e.g., between a mass and a disk due to the deformation of the disk [66]. In [67], experimental evidence of instability caused by a frictional follower force is provided. The follower force characteristic of the friction force causes the generalized force direction to be a function of the generalized coordinates $\boldsymbol{q}$. A frictional follower force can be realized as shown in Fig. 13d. The model consists of a double pendulum with massless rods connected via rotational springs. At the tip of the pendulum, a wheel with negligible mass is mounted to the pendulum such that it can spin freely around its axis. The wheel is in contact with a belt moving with constant velocity. The isotropic Coulomb friction force λ_r acting at the contact point of the wheel and the belt is assumed to be transmitted to the pendulum only in axial direction of the wheel, which causes the generalized force direction $\boldsymbol{w}_r$ to be nonconstant. In the following, systems without the Stribeck effect and with a constant normal force as well as a constant generalized force direction are considered.

4.2 Stability of systems with anisotropic friction

Consider the autonomous differential inclusion

$$\dot{\boldsymbol{x}}(t) \in \mathscr{F}\left(\boldsymbol{x}(t)\right), \tag{74}$$

with the state vector $\boldsymbol{x}(t) \in \mathbb{R}^r$. The set of admissible states is called $\mathscr{A}$. A solution $\boldsymbol{x}(t) = \boldsymbol{\varphi}(t, t_0, \boldsymbol{x}_0)$ of the differential inclusion with initial condition $\boldsymbol{x}_0 \in \mathscr{A}$ is an absolutely continuous function $\boldsymbol{x}: \mathbb{R} \to \mathbb{R}^r$ which fulfills Eq. (74) for almost all $t \geq 0$. Statements on the stability of all solutions can be made. If all solution curves in forward time remain close to their neighboring solutions, it is referred to as incremental stability (see [42]).

Definition 17 (*Incremental Stability of a Differential Inclusion*) The differential inclusion Eq. (74) is called *incrementally stable* if for all $t_0 \in \mathbb{R}$, arbitrary admissible initial conditions $\boldsymbol{x}_1(t_0),\ \boldsymbol{x}_2(t_0) \in \mathscr{A}$ and for all corresponding solution curves $\boldsymbol{x}_1(t) = \boldsymbol{\varphi}(t, t_0, \boldsymbol{x}_1(t_0))$ as well as $\boldsymbol{x}_2(t) = \boldsymbol{\varphi}(t, t_0, \boldsymbol{x}_2(t_0))$, it holds that for each $\epsilon > 0$ there exists a $\delta = \delta(\epsilon)$ such that $\|\boldsymbol{x}_1(t_0) - \boldsymbol{x}_2(t_0)\| < \delta$ implies $\|\boldsymbol{x}_1(t) - \boldsymbol{x}_2(t)\| < \epsilon$ for almost all $t \geq 0$.

In this section, the effect of anisotropic friction laws on the stability of sliding motion is analyzed. To date, no literature exists that specifically studies the stability properties of systems with anisotropic friction. To eliminate all factors being capable of causing friction-induced instability for isotropic friction, a system having one frictional contact with

- Constant normal force,
- Constant generalized force direction,
- No Stribeck effect,

is considered, which excludes all mechanisms of self-excitation mentioned before. In the following, a minimal mechanical model to analyze the effect of anisotropic friction is presented.

Figure 14a shows a mass constrained by two linear springs, sliding on a horizontal belt having anisotropic friction properties. The top view of the model is depicted in Fig. 14b. The sliding body is modeled as a point mass on a surface moving constantly with velocity v. The generalized coordinates $\boldsymbol{q} = [x\ y]^{\mathrm{T}}$ are oriented parallel to the axes $\mathbf{e}_{T_1}$ and $\mathbf{e}_{T_2}$. The equation of motion of the system is given as

$$\boldsymbol{M}\ddot{\boldsymbol{q}} + \boldsymbol{K}\boldsymbol{q} = \boldsymbol{W}_T \boldsymbol{\lambda}_T, \tag{75}$$

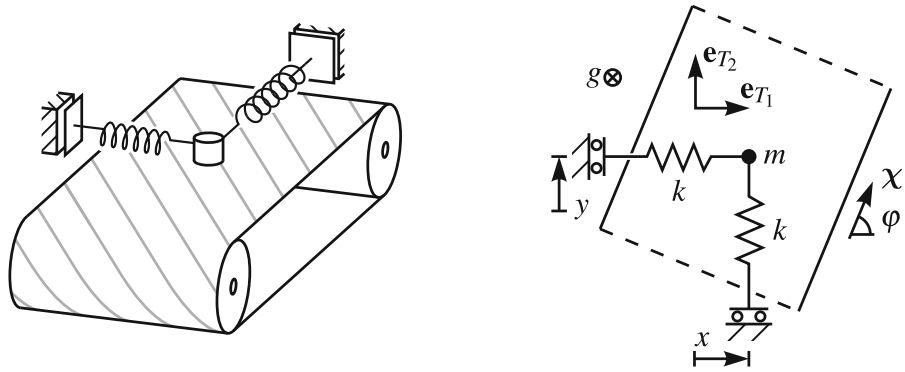

Fig. 14 **a** Mass on belt with anisotropic friction properties. **b** Two degree of freedom model of the mass on belt system

with the diagonal system matrices and belt velocity vector $\boldsymbol{\chi}$

$$\boldsymbol{M} = \begin{bmatrix} m & 0 \\ 0 & m \end{bmatrix}, \quad \boldsymbol{K} = \begin{bmatrix} k & 0 \\ 0 & k \end{bmatrix}, \quad \boldsymbol{W}_T = \begin{bmatrix} 1 & 0 \\ 0 & 1 \end{bmatrix},$$
$$\boldsymbol{\chi} = \begin{bmatrix} v\cos\varphi \\ v\sin\varphi \end{bmatrix}. \tag{76}$$

The relative sliding velocity $\boldsymbol{\gamma}_T$ is given by the motion of the mass and the motion of the belt as $\boldsymbol{\gamma}_T = \boldsymbol{W}_T^{\mathrm{T}}\dot{\boldsymbol{q}} - \boldsymbol{\chi}$. The matrix of the generalized force direction $\boldsymbol{W}_T$, defined by $\boldsymbol{W}_T = (\partial\boldsymbol{\gamma}_T/\partial\dot{\boldsymbol{q}})^{\mathrm{T}}$, in this case is simply the identity matrix. In the following, different anisotropic friction laws are implemented for the friction force $\boldsymbol{\lambda}_T$. In all cases, the normal force resulting from gravity is constant, $\lambda_N = mg$. For vanishing generalized velocities and accelerations, i.e., $\dot{\boldsymbol{q}} = \ddot{\boldsymbol{q}} = \boldsymbol{0}$, the system is at the equilibrium $\boldsymbol{q}_{\mathrm{eq}} = \boldsymbol{K}^{-1}\boldsymbol{W}_T\boldsymbol{\lambda}_T$. Since the belt is moving continuously ($\boldsymbol{\chi} \neq \boldsymbol{0}$), the relative sliding velocity $\boldsymbol{\gamma}_T$ is nonzero for $\dot{\boldsymbol{q}} = \boldsymbol{0}$ so the equilibrium is not in the stick phase. We will now consider different types of anisotropic friction and discuss the stability properties.

First, the associated Coulomb friction law specified in Definition 12, $\boldsymbol{\gamma}_T \in \mathcal{N}_{\mathscr{C}}(-\boldsymbol{\lambda}_T)$, is considered. Here, no additional restrictions on the shape of the force reservoir $\mathscr{C}$ other than convexity are made.

Theorem 1 (Stability for the associated Coulomb friction law) *The differential inclusion given by the mechanical system Eq. (75) in combination with the associated Coulomb friction law is incrementally stable. Consequently, equilibria of the system are stable.*

Proof From Proposition 4, it is known that the associated Coulomb friction law is maximal monotone. Therefore, for all pairs $(\boldsymbol{\gamma}_T, \boldsymbol{\lambda}_T)$ and $(\boldsymbol{\gamma}_T^*, \boldsymbol{\lambda}_T^*)$, the monotonicity condition

$$-(\boldsymbol{\lambda}_T - \boldsymbol{\lambda}_T^*)^{\mathrm{T}}(\boldsymbol{\gamma}_T - \boldsymbol{\gamma}_T^*) \geq 0 \tag{77}$$

from Definition 13(i) holds. We choose two arbitrary solutions of the differential inclusion, $\boldsymbol{q}_{\mathrm{I}}(t)$ and $\boldsymbol{q}_{\mathrm{II}}(t)$. Incremental stability (see Definition 17) can be proven by analyzing the distance between the two solutions. Introducing the incremental Lyapunov candidate function with terms similar to the kinetic and potential energy of the system as a function of the position and velocity error between the two solutions gives

$$V = \frac{1}{2}\left(\dot{\boldsymbol{q}}_{\mathrm{I}} - \dot{\boldsymbol{q}}_{\mathrm{II}}\right)^{\mathrm{T}}\boldsymbol{M}\left(\dot{\boldsymbol{q}}_{\mathrm{I}} - \dot{\boldsymbol{q}}_{\mathrm{II}}\right) + \frac{1}{2}\left(\boldsymbol{q}_{\mathrm{I}} - \boldsymbol{q}_{\mathrm{II}}\right)^{\mathrm{T}}\boldsymbol{K}\left(\boldsymbol{q}_{\mathrm{I}} - \boldsymbol{q}_{\mathrm{II}}\right). \tag{78}$$

Only if the two solutions are identical, it holds that $V = 0$. Since $\boldsymbol{M}$ and $\boldsymbol{K}$ are positive definite, the Lyapunov candidate function V is positive definite. Taking the time-derivative and substitution of Eq. (75) leads to

$$\begin{aligned} \dot{V} &= \left(\dot{\boldsymbol{q}}_{\mathrm{I}} - \dot{\boldsymbol{q}}_{\mathrm{II}}\right)^{\mathrm{T}}\left(\boldsymbol{M}\left(\ddot{\boldsymbol{q}}_{\mathrm{I}} - \ddot{\boldsymbol{q}}_{\mathrm{II}}\right) + \boldsymbol{K}\left(\boldsymbol{q}_{\mathrm{I}} - \boldsymbol{q}_{\mathrm{II}}\right)\right) \\ &= \left(\dot{\boldsymbol{q}}_{\mathrm{I}} - \dot{\boldsymbol{q}}_{\mathrm{II}}\right)^{\mathrm{T}}\left(\boldsymbol{W}_T\boldsymbol{\lambda}_{T_{\mathrm{I}}} - \boldsymbol{W}_T\boldsymbol{\lambda}_{T_{\mathrm{II}}}\right) \\ &= \left(\boldsymbol{W}_T^{\mathrm{T}}\left(\dot{\boldsymbol{q}}_{\mathrm{I}} - \dot{\boldsymbol{q}}_{\mathrm{II}}\right)\right)^{\mathrm{T}}\left(\boldsymbol{\lambda}_{T_{\mathrm{I}}} - \boldsymbol{\lambda}_{T_{\mathrm{II}}}\right) \\ &= \left(\boldsymbol{\gamma}_{T_{\mathrm{I}}} - \boldsymbol{\gamma}_{T_{\mathrm{II}}}\right)^{\mathrm{T}}\left(\boldsymbol{\lambda}_{T_{\mathrm{I}}} - \boldsymbol{\lambda}_{T_{\mathrm{II}}}\right), \end{aligned} \tag{79}$$

where in the last step by subtracting the two solutions the velocity of the belt $\boldsymbol{\chi}$ cancels out. From the monotonicity condition of the force law Eq. (77) it follows that $\dot{V} \leq 0$. Therefore, V is a Lyapunov function which cannot increase over time. This means that the distance

between two solutions is never increasing, i.e., the system is incrementally stable. Since for one of the two solutions the equilibrium $\boldsymbol{q}_{\text{eq}}$ can be taken, stability of the equilibrium is proven. Note that attractivity of the equilibrium does not directly follow and depends on additional damping in the system. □

Anisotropic friction modeled with the associated Coulomb friction law is therefore never responsible for friction-induced instability of mechanical systems given in the form of Eq. (75). Of course, instability can still arise if in addition one of the effects described in Sect. 4.1 is taken into account. The incremental stability result in the associated case directly follows from the maximal monotonicity property and an equivalent conclusion can also be found in [68] in which Lur'e systems with a maximal monotone operator in the feedback loop are considered. In the following, we will consider friction laws which do not enjoy the maximal monotonicity property and show that this can lead to instability.

We analyze the stability of the equilibrium of the system given in Eq. (75) in combination with the extended normal cone inclusion friction law. Anisotropic friction is shown to be a possible cause of friction-induced instability. In the following discussion, the occurrence of instability is demonstrated for sets having a smooth boundary. In addition, a condition of the relationship between the sliding direction and the shape of the force reservoir is given that is responsible for anisotropic friction-induced instability.

From Definition 16, the extended normal cone inclusion friction law is known as

$$\boldsymbol{\gamma}_T \in \mathcal{N}_{\mathscr{D}}(-\alpha\boldsymbol{\lambda}_T) \tag{80}$$

with

$$\alpha = \frac{1}{k_{\mathscr{D}}(-\boldsymbol{\lambda}_T) - k_{\mathscr{C}}(-\boldsymbol{\lambda}_T) + 1}. \tag{81}$$

The formulation is equivalent to $-\alpha\boldsymbol{\lambda}_T \in \partial\Psi^*_{\mathscr{D}}(\boldsymbol{\gamma}_T)$ (see Eq. (68)). We assume a set $\mathscr{D}$ being strictly convex and having a smooth boundary, i.e., the set has no vertices. The force reservoir $\mathscr{C}$ is assumed to be strictly star-shaped with a smooth boundary. The subdifferential of the support function $\Psi^*_{\mathscr{D}}(\boldsymbol{\gamma}_T)$ for $\boldsymbol{\gamma}_T \neq \boldsymbol{0}$ can then be replaced by the gradient with

$$\nabla\Psi^*_{\mathscr{D}}(\boldsymbol{\gamma}_T) = \left(\frac{\partial\Psi^*_{\mathscr{D}}(\boldsymbol{\gamma}_T)}{\partial\boldsymbol{\gamma}_T}\right)^{\mathrm{T}}, \tag{82}$$

and the friction law is single-valued in the sliding state. For a constant velocity $\boldsymbol{\chi}$ at the contact, an equilibrium must occur during slip. Therefore, the friction force takes a value at the boundary of the force reservoir $\mathscr{C}$, and for the gauge function it holds that $k_{\mathscr{C}}(-\boldsymbol{\lambda}_T) = 1$. Substitution of the friction force

$$-\boldsymbol{\lambda}_T = \frac{1}{\alpha}\nabla\Psi^*_{\mathscr{D}}(\boldsymbol{\gamma}_T) \tag{83}$$

in the positively homogeneous gauge function yields the scaling parameter α during slip as a function of the sliding velocity as $\alpha = k_{\mathscr{C}}(\nabla\Psi^*_{\mathscr{D}}(\boldsymbol{\gamma}_T))$. Consequently, during slip, the friction force is described by the explicit function

$$-\boldsymbol{\lambda}_T = \frac{1}{k_{\mathscr{C}}(\nabla\Psi^*_{\mathscr{D}}(\boldsymbol{\gamma}_T))}\nabla\Psi^*_{\mathscr{D}}(\boldsymbol{\gamma}_T). \tag{84}$$

For an explicit function of the friction force, the equation of motion of the system given by Eq. (75) with a constant matrix of the generalized force direction $\boldsymbol{W}_T$ can be linearized around the equilibrium $\boldsymbol{q}_{\text{eq}}$ giving

$$\boldsymbol{M}\ddot{\boldsymbol{q}} + \boldsymbol{B}\dot{\boldsymbol{q}} + \boldsymbol{K}\left(\boldsymbol{q} - \boldsymbol{q}_{\text{eq}}\right) = \boldsymbol{0}, \tag{85}$$

where

$$\boldsymbol{B} = -\boldsymbol{W}_T\frac{\partial\boldsymbol{\lambda}_T}{\partial\boldsymbol{\gamma}_T}\bigg|_{\dot{\boldsymbol{q}}=\boldsymbol{0}}\boldsymbol{W}_T^{\mathrm{T}}. \tag{86}$$

For the given example of a pointmass on a belt, the matrix $\boldsymbol{W}_T$ is the identity matrix. The matrix $\boldsymbol{B}$ is thus defined by the Jacobian of the friction force,

$$-\frac{\partial\boldsymbol{\lambda}_T}{\partial\boldsymbol{\gamma}_T} = \frac{1}{k_{\mathscr{C}}(\nabla\Psi^*_{\mathscr{D}})}\left[\mathbf{I} - \tilde{\boldsymbol{L}}\right]\boldsymbol{H}, \tag{87}$$

where the argument of the support function is suppressed for brevity. Herein, the matrix $\tilde{\boldsymbol{L}}$ and the Hessian matrix $\boldsymbol{H}$ are given as

$$\tilde{\boldsymbol{L}} = \frac{1}{k_{\mathscr{C}}(\nabla\Psi^*_{\mathscr{D}})}\nabla\Psi^*_{\mathscr{D}}\frac{\partial k_{\mathscr{C}}(\boldsymbol{x})}{\partial\boldsymbol{x}}\bigg|_{\nabla\Psi^*_{\mathscr{D}}}, \quad \boldsymbol{H} = \frac{\partial^2\Psi^*_{\mathscr{D}}}{\partial\boldsymbol{\gamma}_T^2}. \tag{88}$$

To determine the stability properties of the equilibrium, we analyze the eigenvalues of the matrix $\boldsymbol{B}$. Each part of the matrix $\boldsymbol{B}$ is considered separately.

First, the eigenvalues of the matrix $\tilde{\boldsymbol{L}} \in \mathbb{R}^{2\times 2}$ are determined. The matrix consists of an outer product of nonzero vectors multiplied by a scalar factor being greater than zero. Consequently, the matrix is of rank one. One eigenvalue is zero, $l_1^{\tilde{L}} = 0$ and if $\tilde{\boldsymbol{L}}$ is diagonalizable, then the second eigenvalue is given by the trace of the matrix. In general, it holds that $\operatorname{tr}\left(\boldsymbol{x}\boldsymbol{y}^{\mathrm{T}}\right) = \boldsymbol{x}^{\mathrm{T}}\boldsymbol{y}$, and since the gauge function is positively homogeneous of degree one, it holds that

$$\left.\frac{\partial k_{\mathscr{C}}(\boldsymbol{x})}{\partial \boldsymbol{x}}\right|_{\boldsymbol{y}} \boldsymbol{y} = k_{\mathscr{C}}(\boldsymbol{y}). \tag{89}$$

It follows that $l_2^{\tilde{L}} = k_{\mathscr{C}}(\nabla\Psi_{\mathscr{D}}^*)^{-1} k_{\mathscr{C}}(\nabla\Psi_{\mathscr{D}}^*) = 1$. A corresponding eigenvector is given by $\boldsymbol{v}_2^{\tilde{L}} = \boldsymbol{\lambda}_T$ which is verified using Eqs. (84), (88) and (89) giving $\tilde{\boldsymbol{L}}\boldsymbol{\lambda}_T = \boldsymbol{\lambda}_T$. An eigenvector to the zero eigenvalue is called $\boldsymbol{v}_1^{\tilde{L}} = \boldsymbol{w}$. It holds that

$$\tilde{\boldsymbol{L}}\boldsymbol{w} = \boldsymbol{0} \tag{90}$$

$$\Longrightarrow \left.\frac{\partial k_{\mathscr{C}}(\boldsymbol{x})}{\partial \boldsymbol{x}}\right|_{\nabla\Psi_{\mathscr{D}}^*} \boldsymbol{w} = 0. \tag{91}$$

Since the gradient of the gauge function of $\mathscr{C}$ is orthogonal to the boundary of the set, the vector $\boldsymbol{w}$ must be tangent to the boundary.

Next, the matrix $\boldsymbol{L} = \mathbf{I} - \tilde{\boldsymbol{L}}$ is considered.

Proposition 6 *Let $\boldsymbol{v}$ be an eigenvector of the square matrix $\tilde{\boldsymbol{L}}$ with the corresponding eigenvalue l. It holds that $\boldsymbol{v}$ is also an eigenvector of the matrix $\boldsymbol{L} = \mathbf{I} - \tilde{\boldsymbol{L}}$ with the corresponding eigenvalue $(1 - l)$.*

Proof From $\tilde{\boldsymbol{L}}\boldsymbol{v} = l\boldsymbol{v}$ it follows that

$$\boldsymbol{L}\boldsymbol{v} = (\mathbf{I} - \tilde{\boldsymbol{L}})\boldsymbol{v} = \boldsymbol{v} - l\boldsymbol{v} = (1 - l)\boldsymbol{v}. \tag{92}$$

□

With Proposition 6, the eigenvalues and eigenvectors of $\boldsymbol{L}$ are found to be $l_1^{L} = 1, l_2^{L} = 0, \boldsymbol{v}_1^{L} = \boldsymbol{w}, \boldsymbol{v}_2^{L} = \boldsymbol{\lambda}_T$.

The support function of the convex set $\mathscr{D}$ is convex, and the Hessian matrix of a convex function is positive semidefinite. Furthermore, the support function $\Psi_{\mathscr{D}}^*$ is positively homogeneous of degree one, i.e., it holds that $\Psi_{\mathscr{D}}^*(a\boldsymbol{\gamma}_T) = a\Psi_{\mathscr{D}}^*(\boldsymbol{\gamma}_T)$ for all $a > 0$, and differentiation yields

$$\nabla\Psi_{\mathscr{D}}^*(a\boldsymbol{\gamma}_T) = \nabla\Psi_{\mathscr{D}}^*(\boldsymbol{\gamma}_T) \quad \forall a > 0. \tag{93}$$

A Taylor series expansion of the gradient of the support function is given by

$$\nabla\Psi_{\mathscr{D}}^*((1+\epsilon)\boldsymbol{\gamma}_T) = \nabla\Psi_{\mathscr{D}}^*(\boldsymbol{\gamma}_T) + \left.\frac{\partial^2\Psi_{\mathscr{D}}^*}{\partial\boldsymbol{\gamma}_T^2}\right|_{\boldsymbol{\gamma}_T} \epsilon\boldsymbol{\gamma}_T + \mathscr{O}(\epsilon^2). \tag{94}$$

In addition, from Eq. (93) it follows that

$$\nabla\Psi_{\mathscr{D}}^*((1+\epsilon)\boldsymbol{\gamma}_T) = \nabla\Psi_{\mathscr{D}}^*(\boldsymbol{\gamma}_T) \quad \forall \epsilon > 0. \tag{95}$$

From Eqs. (94) and (95) we can conclude that

$$\left.\frac{\partial^2\Psi_{\mathscr{D}}^*}{\partial\boldsymbol{\gamma}_T^2}\right|_{\boldsymbol{\gamma}_T} \epsilon\boldsymbol{\gamma}_T + \mathscr{O}(\epsilon^2) = \boldsymbol{0} \quad \forall \epsilon > 0, \tag{96}$$

which implies

$$\frac{\partial^2\Psi_{\mathscr{D}}^*}{\partial\boldsymbol{\gamma}_T^2}\boldsymbol{\gamma}_T = \boldsymbol{0}. \tag{97}$$

Hence, $\boldsymbol{\gamma}_T$ is an eigenvector to the zero eigenvalue of the Hessian matrix. Since the Hessian matrix is symmetric, all eigenvalues are real and the eigenvectors are orthogonal. Therefore, a second eigenvalue $l_2^{H} > 0$ and an eigenvector $\boldsymbol{\gamma}_T^{\perp}$ orthogonal to $\boldsymbol{\gamma}_T$ must exist.

The scalar factor $k_{\mathscr{C}}(\nabla\Psi_{\mathscr{D}}^*) > 0$ in Eq. (87) has no influence on the sign of the eigenvalues and can be neglected in the stability analysis. In summary, so far, we have

$$\boldsymbol{L}\boldsymbol{\lambda}_T = \boldsymbol{0}, \quad \boldsymbol{L}\boldsymbol{w} = \boldsymbol{w}, \quad \boldsymbol{H}\boldsymbol{\gamma}_T = \boldsymbol{0}, \quad \boldsymbol{H}\boldsymbol{\gamma}_T^{\perp} = l_2^{H}\boldsymbol{\gamma}_T^{\perp} \tag{98}$$

with $l_2^{H} > 0$. Finally, the eigenvalues of the matrix $\boldsymbol{L}\boldsymbol{H}$ are studied. From $\boldsymbol{H}\boldsymbol{\gamma}_T = \boldsymbol{0}$, it directly follows that $\boldsymbol{L}\boldsymbol{H}\boldsymbol{\gamma}_T = \boldsymbol{0}$. Thus, the first eigenvalue of the matrix product is zero and the corresponding eigenvector is $\boldsymbol{\gamma}_T$. Since the extended normal cone inclusion friction law is strictly dissipative, i.e., $-\boldsymbol{\lambda}_T^{\mathrm{T}}\boldsymbol{\gamma}_T > 0$ holds for all $\boldsymbol{\gamma}_T \neq \boldsymbol{0}$, the condition

$$\nexists k \in \mathbb{R} : \boldsymbol{\gamma}_T^{\perp} = k\boldsymbol{\lambda}_T \tag{99}$$

is fulfilled. In addition, from the first two equations of Eq. (98), we obtain that

$$\nexists k \in \mathbb{R} : \boldsymbol{w} = k\boldsymbol{\lambda}_T, \tag{100}$$

which describes that the friction force $\boldsymbol{\lambda}_T$ can not be collinear to the vector $\boldsymbol{w}$ which is nonzero and tangent to the force reservoir. This is related to the assumption that the force reservoir is strictly star-shaped.

Proposition 7 *Let $\boldsymbol{L} \in \mathbb{R}^{2\times 2}$ and $\boldsymbol{H} \in \mathbb{R}^{2\times 2}$ be square matrices and let Eqs. (98)–(100) be fulfilled. It holds that the nullspace of the matrix product $\boldsymbol{LH}$ is of dimension one.*

Proof The vector $\boldsymbol{\gamma}_T$ is in the nullspace of $\boldsymbol{LH}$. Consider another vector $\boldsymbol{v} = a_1\boldsymbol{\gamma}_T + a_2\boldsymbol{\gamma}_T^{\perp}$ with $a_2 \neq 0$. With Eq. (98) it follows that

$$\begin{aligned}\boldsymbol{LH}\boldsymbol{v} &= \boldsymbol{LH}(a_1\boldsymbol{\gamma}_T + a_2\boldsymbol{\gamma}_T^{\perp})\\ &= a_2 l_2^{\boldsymbol{H}}\boldsymbol{L}\boldsymbol{\gamma}_T^{\perp}\\ &= a_2 l_2^{\boldsymbol{H}}\boldsymbol{L}(b_1\boldsymbol{\lambda}_T + b_2\boldsymbol{w})\\ &= a_2 b_2 l_2^{\boldsymbol{H}}\boldsymbol{w} \neq \boldsymbol{0},\end{aligned} \tag{101}$$

where the vector $\boldsymbol{\gamma}_T^{\perp}$ can be expressed by the components in $\boldsymbol{\lambda}_T$ and $\boldsymbol{w}$ direction due to Eq. (100), and $b_2 \neq 0$ because of Eq. (99). □

In the case of $\boldsymbol{\gamma}_T$ and $\boldsymbol{w}$ being parallel, i.e., the relative sliding velocity $\boldsymbol{\gamma}_T$ is tangent to the boundary of the force reservoir, the following statement on the algebraic multiplicity of the zero eigenvalue can be made.

Proposition 8 *Let $\boldsymbol{L} \in \mathbb{R}^{2\times 2}$ and $\boldsymbol{H} \in \mathbb{R}^{2\times 2}$ be square matrices and let Eqs. (98)–(100) be fulfilled. If $\exists c \neq 0 : \boldsymbol{\gamma}_T = c\boldsymbol{w}$, then the zero eigenvalue of the matrix $\boldsymbol{LH}$ has the algebraic multiplicity two.*

Proof From Proposition 7, we know that the geometric multiplicity of the zero eigenvalue must be one. The vector $\boldsymbol{\gamma}_T$ is an eigenvector of $\boldsymbol{LH}$ with eigenvalue zero. From Eq. (101) and $\boldsymbol{\gamma}_T = c\boldsymbol{w}$, with $c \neq 0$, it follows that for every vector $\boldsymbol{v} \in \mathbb{R}^2$

$$\boldsymbol{LH}\boldsymbol{v} = \beta\boldsymbol{w} = \frac{\beta}{c}\boldsymbol{\gamma}_T \tag{102}$$

and, hence, $(\boldsymbol{LH})^2\boldsymbol{v} = \boldsymbol{0}$. If $\boldsymbol{\gamma}_T = c\boldsymbol{w}$, every vector is a generalized eigenvector. □

In the following, the tangent cone $\mathscr{T}_{\mathscr{C}}$ of the force reservoir $\mathscr{C}$, which is given by Definition 7, is used.

Proposition 9 *Let $\boldsymbol{L} \in \mathbb{R}^{2\times 2}$ and $\boldsymbol{H} \in \mathbb{R}^{2\times 2}$ be square matrices and let Eqs. (98)–(100) be fulfilled. The vector $\boldsymbol{w}$ is an eigenvector of the matrix $\boldsymbol{LH}$. For the corresponding eigenvalue it holds that if $\boldsymbol{\gamma}_T \in \mathscr{T}_{\mathscr{C}}(-\boldsymbol{\lambda}_T)$, then the eigenvalue $l_2^{\boldsymbol{LH}}$ is non-positive. The eigenvalue is negative if*

$$\boldsymbol{\gamma}_T \in \operatorname{int} \mathscr{T}_{\mathscr{C}}(-\boldsymbol{\lambda}_T) \tag{103}$$

and strictly positive if $\boldsymbol{\gamma}_T \notin \mathscr{T}_{\mathscr{C}}(-\boldsymbol{\lambda}_T)$.

Proof We first consider the case $\exists c \neq 0 : \boldsymbol{\gamma}_T = c\,(-\boldsymbol{\lambda}_T)$, i.e., the relative sliding velocity is collinear to the friction force. Therefore, it holds that $\boldsymbol{\gamma}_T \notin \mathscr{T}_{\mathscr{C}}(-\boldsymbol{\lambda}_T)$. From the dissipativity of the friction law it is known that $c > 0$. Let

$$\boldsymbol{w} = a_1\boldsymbol{\gamma}_T + a_2\boldsymbol{\gamma}_T^{\perp} = -a_1 c\boldsymbol{\lambda}_T + a_2\boldsymbol{\gamma}_T^{\perp} \tag{104}$$

$$\implies \boldsymbol{\gamma}_T^{\perp} = \frac{1}{a_2}\boldsymbol{w} + \frac{a_1}{a_2}c\boldsymbol{\lambda}_T, \tag{105}$$

where $a_2 \neq 0$ holds due to Eq. (100). Similar reasoning as shown in Eq. (101) results in $\boldsymbol{LH}\boldsymbol{w} = l_2^{\boldsymbol{H}}\boldsymbol{w}$. Thus, in the case of collinear sliding velocity and friction force, $\boldsymbol{w}$ is an eigenvector with strictly positive eigenvalue.

Next, we consider the case $c_2 \neq 0$ and

$$\boldsymbol{\gamma}_T = c_1(-\boldsymbol{\lambda}_T) + c_2\boldsymbol{w} \tag{106}$$

$$\implies \boldsymbol{w} = \frac{1}{c_2}\boldsymbol{\gamma}_T + \frac{c_1}{c_2}\boldsymbol{\lambda}_T. \tag{107}$$

The friction force can be written as:

$$-\boldsymbol{\lambda}_T = d_1\boldsymbol{\gamma}_T + d_2\boldsymbol{\gamma}_T^{\perp} \tag{108}$$

$$\implies \boldsymbol{\gamma}_T^{\perp} = -\frac{1}{d_2}\boldsymbol{\lambda}_T - \frac{d_1}{d_2}\boldsymbol{\gamma}_T, \tag{109}$$

where $d_2 \neq 0$ follows from Eq. (106) with $c_2 \neq 0$. The signs of c_2 and d_2 depend on the arbitrarily chosen positive direction of the vectors $\boldsymbol{w}$ and $\boldsymbol{\gamma}_T^{\perp}$ (see Fig. 15a) and have no influence on the following consideration. From the dissipation rate $-\boldsymbol{\lambda}_T^{\mathrm{T}}\boldsymbol{\gamma}_T = d_1\|\boldsymbol{\gamma}_T\|^2 > 0$, we obtain $d_1 > 0$. Consecutive substitution of Eqs. (106)–(109) together with Eq. (98) yields

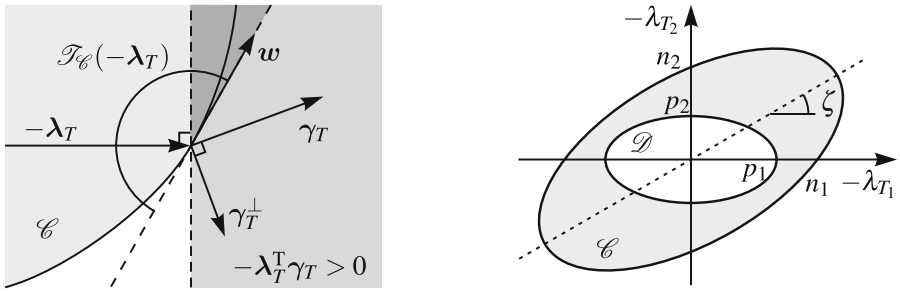

Fig. 15 **a** Relationship between the direction of the friction force $\boldsymbol{\lambda}_T$, sliding velocity $\boldsymbol{\gamma}_T$ and eigenvector $\boldsymbol{w}$ of the damping matrix. **b** Ellipsoidal sets with rotated force reservoir $\mathscr{C}$

$$
\begin{aligned}
\boldsymbol{L}\boldsymbol{H}\boldsymbol{w} &= \boldsymbol{L}\boldsymbol{H}\left(\frac{1}{c_2}\boldsymbol{\gamma}_T + \frac{c_1}{c_2}\boldsymbol{\lambda}_T\right)\\
&= \boldsymbol{L}\boldsymbol{H}\left(\frac{1}{c_2}\boldsymbol{\gamma}_T - \frac{c_1}{c_2}\left(d_1\boldsymbol{\gamma}_T + d_2\boldsymbol{\gamma}_T^{\perp}\right)\right)\\
&= -\,d_2\frac{c_1}{c_2}l_2^{\boldsymbol{H}}\boldsymbol{L}\boldsymbol{\gamma}_T^{\perp}\\
&= -\,d_2\frac{c_1}{c_2}l_2^{\boldsymbol{H}}\boldsymbol{L}\left(-\frac{1}{d_2}\boldsymbol{\lambda}_T - \frac{d_1}{d_2}\boldsymbol{\gamma}_T\right)\\
&= -\,\frac{c_1}{c_2}l_2^{\boldsymbol{H}}\boldsymbol{L}\left(-\boldsymbol{\lambda}_T - d_1\left(-c_1\boldsymbol{\lambda}_T + c_2\boldsymbol{w}\right)\right)\\
&= c_1 d_1 l_2^{\boldsymbol{H}}\boldsymbol{w}. \qquad (110)
\end{aligned}
$$

It follows that $\boldsymbol{w}$ is an eigenvector of $\boldsymbol{L}\boldsymbol{H}$. Since $d_1 > 0$ and $l_2^{\boldsymbol{H}} > 0$, the sign of the corresponding eigenvalue only depends on the parameter c_1. The eigenvector $\boldsymbol{w}$ is tangent to the boundary of the force reservoir $\mathscr{C}$ (see Fig. 15a). Hence, for $c_1 < 0$ in Eq. (106), the sliding direction is in the interior of the tangent cone of the force reservoir at $-\boldsymbol{\lambda}_T$ and the eigenvalue being the product $c_1 d_1 l_2^{\boldsymbol{H}}$ is negative. In contrast, if c_1 is strictly positive, then the sliding direction is not in the tangent cone and the eigenvalue is strictly positive. If the sliding direction is parallel to the boundary of the force reservoir ($c_1 = 0$), then the zero eigenvalue has algebraic multiplicity two (see Proposition 8). □

The statement on the sign of the nonzero eigenvalue given in Proposition 9 also holds true for the sign of the nonzero eigenvalue of the Jacobian matrix given in Eq. (87). In conclusion, we have that the matrix $\boldsymbol{B}$ defined by Eq. (86), which is in general nonsymmetric, is always singular, even if $\boldsymbol{W}_T$ has full rank. This is the case because, due to the assumption of Coulomb friction without Stribeck effect, the friction force only depends on the direction of sliding and not on its magnitude. The zero eigenvalue always corresponds to the eigenvector $\boldsymbol{\gamma}_T$. Furthermore, the nonzero eigenvalue of $\boldsymbol{B}$ is shown to be negative for sliding directions in the interior of the tangent cone of the force reservoir. This is impossible in the case of an associated or collinear friction law. However, with the extended normal cone inclusion friction law, it is possible, even for convex sets $\mathscr{C}$ and $\mathscr{D}$ as shown later in this work.

We can separate the generally nonsymmetric matrix $\boldsymbol{B}$ into the symmetric damping matrix $\boldsymbol{D}$ and skew-symmetric gyroscopic matrix $\boldsymbol{G}$ by

$$
\boldsymbol{D} = \frac{1}{2}\left(\boldsymbol{B} + \boldsymbol{B}^{\mathrm{T}}\right), \quad \boldsymbol{G} = \frac{1}{2}\left(\boldsymbol{B} - \boldsymbol{B}^{\mathrm{T}}\right). \qquad (111)
$$

In the case of $\boldsymbol{B}$ having a nonzero eigenvalue, i.e., $\boldsymbol{\gamma}_T$ is not tangent to the boundary of the force reservoir, the matrix $\boldsymbol{B}$ is diagonalizable and the trace of $\boldsymbol{B}$ is given as the sum of the eigenvalues of $\boldsymbol{B}$. For $\boldsymbol{B}$ having a negative eigenvalue, we have $\operatorname{tr}\boldsymbol{B} = \operatorname{tr}\boldsymbol{D} < 0$. In general, no statement on the stability can be made from the trace of the damping matrix. However, it is possible to formulate the following sufficient condition for the instability of an equilibrium (see [69]).

Proposition 10 (Sufficient Condition for Instability) *Let the equation of motion of a mechanical system be given by Eq.* (85). *The equilibrium of the system is unstable if the condition*

$$
\operatorname{tr}\left(\boldsymbol{M}^{-1}\boldsymbol{B}\right) = \operatorname{tr}\left(\boldsymbol{M}^{-1}\boldsymbol{D}\right) < 0 \qquad (112)
$$

is fulfilled.

Proof The system can be rewritten in first-order form with the state vector $\boldsymbol{x} = \left[\boldsymbol{q}^{\mathrm{T}}\ \dot{\boldsymbol{q}}^{\mathrm{T}}\right]^{\mathrm{T}}$ and the system matrix

$$
\boldsymbol{A} = \begin{bmatrix} \mathbf{0} & \mathbf{I} \\ -\boldsymbol{M}^{-1}\boldsymbol{K} & -\boldsymbol{M}^{-1}\boldsymbol{B} \end{bmatrix}. \qquad (113)
$$

as $\dot{\boldsymbol{x}} = \boldsymbol{A}\boldsymbol{x}$. The equilibrium is unstable if the real part of at least one eigenvalue of $\boldsymbol{A}$ is strictly positive [70]. If Eq. (112) holds, then $\mathrm{tr}\boldsymbol{A} = -\mathrm{tr}\left(\boldsymbol{M}^{-1}\boldsymbol{B}\right) = -\mathrm{tr}\left(\boldsymbol{M}^{-1}\boldsymbol{D}\right) > 0$. With the trace being the sum of all eigenvalues, there must be at least one eigenvalue with strictly positive real part. □

We have that the symmetric mass matrix is positive definite and the eigenvalues of $\boldsymbol{B}$ are zero and a negative scalar. But since $\boldsymbol{B}$ is in general nonsymmetric and its symmetric part $\boldsymbol{D}$ can have positive and negative eigenvalues, it is problematic to exploit trace inequalities or the similarity-invariance of the trace for proving general statements on the stability. However, for the general class of systems having a mass matrix in the form of a scalar multiple of the identity matrix, instability of the equilibrium can be proven if $\boldsymbol{B}$ has a negative eigenvalue. This is the case in the mass on belt system given in Eq. (75).

Proposition 11 *Let a linearized mechanical system be described by Eq. (85) and let $\boldsymbol{M} = m\mathbf{I}$ with $m > 0$. If the only nonzero eigenvalue of $\boldsymbol{B}$ is negative, then the equilibrium $\boldsymbol{q}_{\mathrm{eq}}$ is unstable.*

Proof The negative eigenvalue of the matrix $\boldsymbol{B}$ causes the trace of $\boldsymbol{B}$ to be negative.

For the admissible form of the mass matrix, we can conclude that the instability condition Eq. (112) is fulfilled. □

Finally, a theorem stating the instability of an equilibrium for a system with anisotropic frictional behavior can be given if the extended normal cone inclusion friction law is considered.

Theorem 2 (Anisotropic Friction-Induced Instability) *Let a mechanical system with a single contact point with anisotropic Coulomb friction be described by Eq. (75) with $\boldsymbol{M} = m\mathbf{I}$ and $m > 0$. Let the friction force be defined by the extended normal cone inclusion friction law (see Definition 16). If for the relative sliding velocity $\boldsymbol{\gamma}_T \neq \mathbf{0}$ at an equilibrium of the system the friction law yields*

$$\boldsymbol{\gamma}_T \in \mathrm{int}\, \mathscr{T}_{\mathscr{C}}(-\boldsymbol{\lambda}_T), \tag{114}$$

then the equilibrium is unstable.

Proof The theorem follows from Propositions 9 and 11 and the above discussion. □

Theorem 2 proves that even for a constant normal force, a constant matrix of generalized force direction and a constant force reservoir, an anisotropic friction law can cause friction-induced instability.

Numerical Example

To illustrate the occurrence of anisotropic friction-induced instability with the extended normal cone inclusion friction law, the friction law with ellipsoidal sets $\mathscr{C}$ and $\mathscr{D}$ is considered as an example [71]. The dynamics is given by the mass on belt system described by Eqs. (75) and (76). For ellipsoidal sets centered around the origin and having parallel principal axes, the eigenvalues of the matrix $\boldsymbol{B}$, defined by Eq. (86), never have a negative real part. Instead, we consider an ellipsoidal force reservoir rotated around the origin with angle ζ as shown in Fig. 15b. The gauge and support functions of the sets are given with their positive axis intercepts n_1, n_2, p_1, p_2 and rotation parameter ν as

$$k_{\mathscr{C}}(-\boldsymbol{\lambda}_T) = \sqrt{\left(\frac{\lambda_{T_1}}{n_1}\right)^2 + \left(\frac{\lambda_{T_2}}{n_2}\right)^2 + \nu\lambda_{T_1}\lambda_{T_2}}, \tag{115}$$

$$k_{\mathscr{D}}(-\boldsymbol{\lambda}_T) = \sqrt{\left(\frac{\lambda_{T_1}}{p_1}\right)^2 + \left(\frac{\lambda_{T_2}}{p_2}\right)^2}, \tag{116}$$

$$\Psi^*_{\mathscr{D}}(\boldsymbol{\gamma}_T) = \sqrt{\left(p_1\gamma_{T_1}\right)^2 + \left(p_2\gamma_{T_2}\right)^2}. \tag{117}$$

For an ellipsoidal force reservoir, the condition $|\nu| < 2/(n_1 n_2)$ has to be fulfilled. An eigenvalue analysis of the resulting singular damping matrix $\boldsymbol{B}$ of the linearized system yields that the nonzero eigenvalue becomes negative for certain relative sliding directions if

$$|\nu| > \frac{p_1 p_2}{p_1^2 + p_2^2}\frac{4}{n_1 n_2}. \tag{118}$$

For $p_1 = p_2$, the two conditions for ν coincide. Thus, for the collinear friction law for which the set $\mathscr{D}$ is circular, anisotropic friction-induced instability is impossible. Whenever $p_1 \neq p_2$, the conditions can be fulfilled. Let the semi-axes ratios of both ellipsoidal sets be 3/1. The critical range of the rotation angle ζ of the force reservoir, allowing for a negative eigenvalue is then found to be approximately $17° < \zeta < 73°$. In the following, $\zeta = 30°$ is considered. The friction law does not guarantee instability for all sliding directions. Sta-

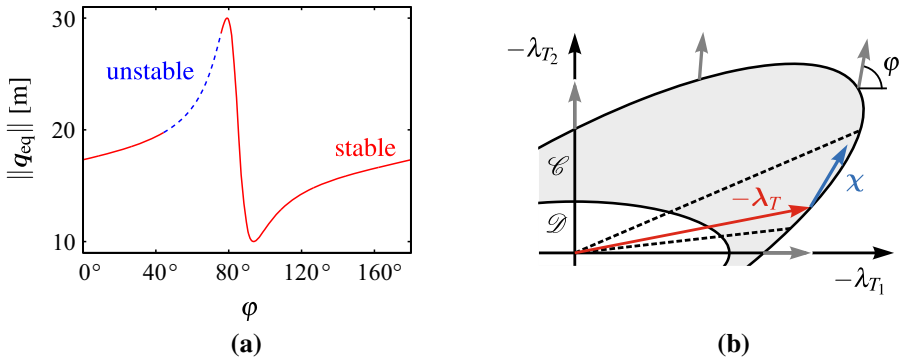

Fig. 16 Stability analysis for a rotation angle of the force reservoir $\zeta = 30°$. **a** Bifurcation diagram with the angle of the belt direction as parameter. **b** Graphical representation of the friction law

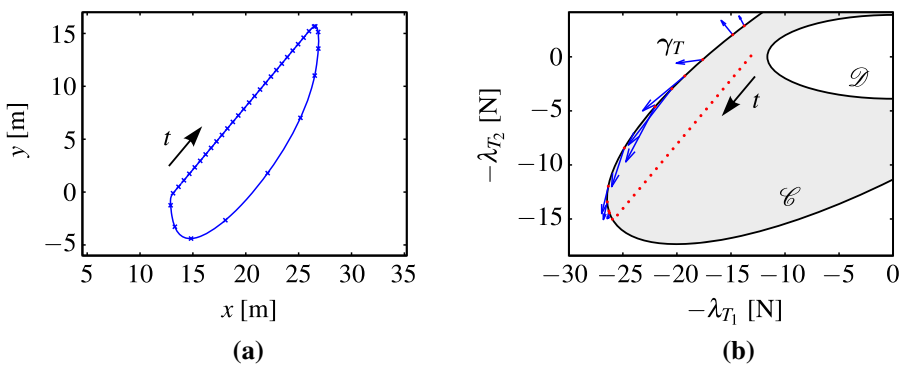

Fig. 17 **a** Limit cycle of the displacement of the mass on the moving belt for $\varphi = 50°$. **b** Friction force and relative sliding velocity of the mass during one cycle and friction force reservoir $\mathscr{C}$

bility of the equilibrium depends on the direction of the belt movement defined by the angle φ (see Fig. 14b). A bifurcation diagram showing the stability of the equilibrium as a function of the bifurcation parameter φ is plotted in Fig. 16a. Instability occurs in the critical range of approximately $44° < \varphi < 76°$. Figure 16b demonstrates that in the critical range of φ, the relative sliding velocity at the equilibrium $\boldsymbol{\gamma}_T = \boldsymbol{\chi}$ is in the tangent cone of the force reservoir, which agrees to Theorem 2. For the limit values of the critical range of φ, the relative sliding direction is tangent to the boundary of the force reservoir at the corresponding value of the friction force.

We consider the mass on belt system with unit mass and stiffness matrix and an ellipsoidal force reservoir with semi-axes 30 N and 10 N rotated around the origin with $\zeta = 30°$. For angles in the critical range, the equilibrium is unstable. When a small perturbation is applied, the mass on the belt spirals away from the equilibrium position and starts to oscillate. For the example of $\varphi = 50°$, a numerical simulation using Moreau's time-stepping scheme as described in Sect. 2.3, with the extension given in Sect. 3.4, shows that after some time, a limit cycle is reached. The limit cycle in the x-y displacement plane is plotted in Fig. 17a. Since the belt velocity is chosen low ($v = 1$ m/s), the mass sticks to the belt during each cycle, which results in the straight segment of the limit cycle. For higher belt velocities, limit cycles without stiction are observed. In the plot, the position for every eighth time step is marked with a cross. In Fig 17b, the corresponding friction forces and relative sliding velocities are plotted together with the force reservoir $\mathscr{C}$. During the stick phase, the friction force increases and linearly approaches the boundary of the force reservoir, while the relative sliding velocity is zero. When the friction force reaches the boundary, the mass starts to slide and the friction force moves along the boundary of $\mathscr{C}$. At the end of the slip phase, the friction force jumps to a value in the interior of the force reservoir, and the cycle repeats.

5 Experimental analysis of anisotropic friction

Accurate modeling of anisotropic friction relies on detailed experimental data of the frictional behavior

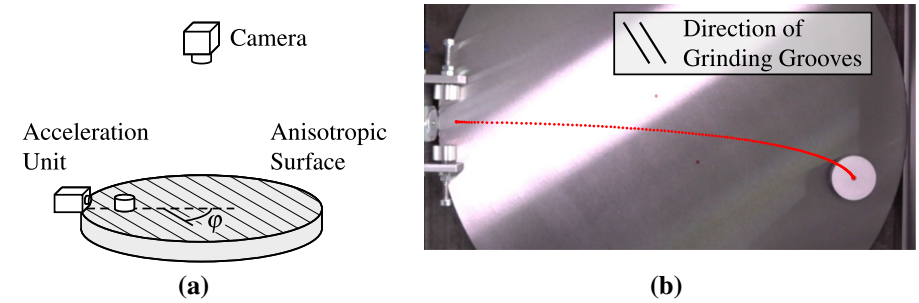

Fig. 18 Tracking of the sliding path of a disk on a horizontal anisotropic surface. **a** Schematic view of the experiment. **b** Top view of the sliding path of a polymer disk on surface ground steel

of materials. This section starts with a discussion of the surface conditions of the surface ground steel specimens considered in the experiments. In Sect. 5.1, an experiment used to study the qualitative behavior of a disk sliding on an anisotropic surface is presented. Section 5.2 deals with the measurement of friction forces with a novel tribometer. Finally, the experimentally obtained data is used to compare different friction laws in Sect. 5.3.

Due to the broad field of application of machined metals in engineering, the experimental work in this paper is focused on the frictional behavior of surface ground steel. Case hardening steel with the material number 1.7139 and the chemical composition 16MnCrS5 is utilized. Since this tool steel has a high wear resistance, it is often used for camshafts, gears and other parts that are subjected to friction and wear. The plain, flat surface is machined using a horizontal-spindle (peripheral) surface grinder. Peripheral grinding produces a straight, parallel pattern of grinding grooves which is expected to cause anisotropic frictional behavior. Using confocal microscopy, the grinding grooves are found to be parallel with a mean spacing of approximately 8 µm and the arithmetic average of the roughness profile orthogonal to the grooves is $R_a = 0.35\,\mu\text{m}$.

5.1 Experimental analysis of sliding paths

To experimentally confirm that the friction force in the case of anisotropic friction is not necessarily collinear to the sliding direction, the sliding paths of disks sliding on a surface having anisotropic friction properties are analyzed. A schematic view of the experimental setup is shown in Fig. 18a.

The anisotropic surface is a horizontal surface ground steel disk, having a diameter of 30 cm. On top of the steel plate, a disk with a diameter of 28 mm and a height of 13 mm is accelerated and slides under the influence of friction until it comes to a stop on the plate. Not the whole bottom surface of the sliding disk is in contact with the steel plate. Instead, three circular contact areas, each having a diameter of 7 mm, are equally distributed on a circle with diameter 21 mm. The material at the contact areas is polyvinyl chloride (PVC) and the weight of the disk is 18 g. The acceleration unit, consisting of a linear solenoid and a centering device, is used to accelerate the disk at a specified angle φ with respect to the direction of the grinding grooves. The initial velocity v_0 of the sliding disk depends on the applied voltage at the solenoid. The sliding path is recorded with a Sony RX10 II camera with a frame rate of 500 fps. For further image processing, the recorded frames are filtered using a two-dimensional Gaussian filter. A red mark centered on the top of the sliding disk is tracked by evaluation of the RGB channels of the images. The convex hull of the detected red pixels of the mark is determined using Delaunay triangulation. To find the center of the mark, a circle is fitted to the convex hull using the method of least squares. Figure 18b shows an example of the tracked points with a time interval of 2 ms between two points and the last frame of the record in the background. From the position of the tracked mark on the top of the sliding disk, the displacement of the disk can be calculated.

Figure 19a shows the resulting sliding paths for the constant angle $\varphi = 47°$ and varying initial velocities v_0. The sliding disk is clearly deflected from a straight line. Higher initial velocities obviously lead to longer sliding paths. In addition, the figure shows that the final sliding direction in all cases is in the direction of the grinding grooves. The same is seen in Fig. 19b for the initial velocity $v_0 = 1.49\,\text{m/s}$ and different angles φ. When the initial sliding velocity is parallel or orthog-

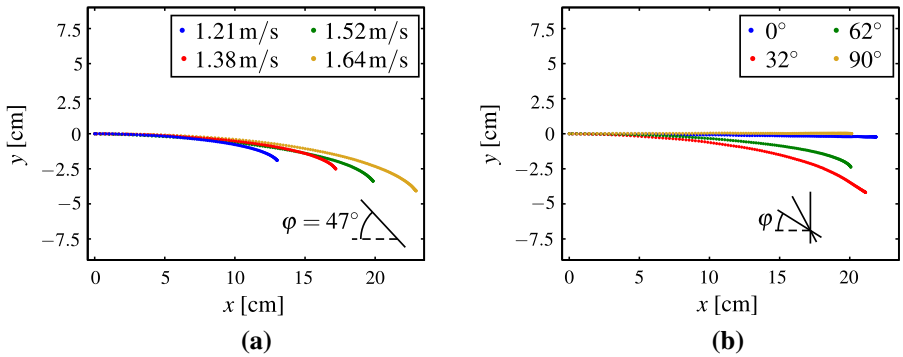

Fig. 19 Measured sliding paths of a PVC disk on a horizontal surface ground steel plate. **a** Results for $\varphi = 47°$ and different initial velocities. **b** Results for $v_0 = 1.49$ m/s and different angles φ

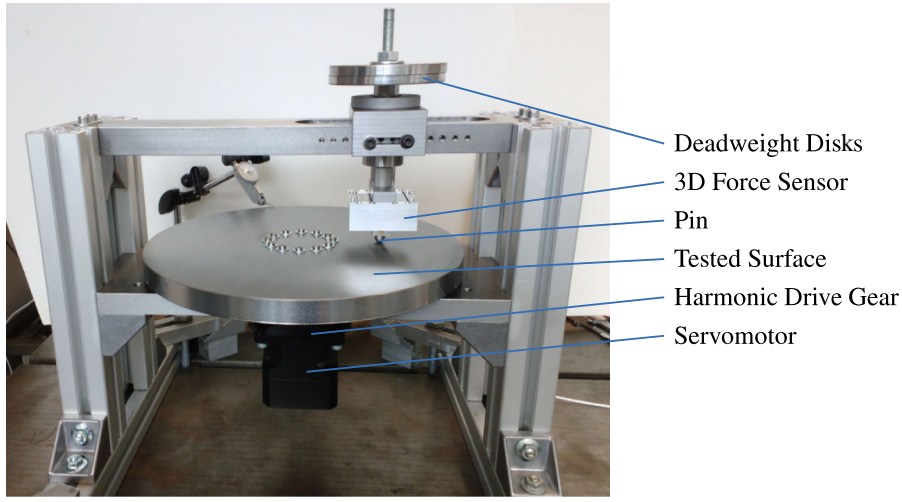

Fig. 20 Experimental pin-on-disk setup for the measurement of friction forces

onal to the grinding grooves, the disk is not deflected. Furthermore, it holds that the sliding path is longer when the disk is sliding parallel to the grinding grooves than when it is sliding orthogonal to them.

The experiments show that the *magnitude* of the friction force depends on the sliding direction. Moreover, the deflection of the sliding disk proves that the *direction* of the friction force is also dependent on the sliding direction. In general, anisotropic friction forces are not collinear to the sliding direction.

5.2 Measurement of friction forces

The previous section is concerned with the qualitative behavior of anisotropic dry friction. Next, an experimental setup to measure the friction forces is described. The experimental results can be used to determine the force reservoir $\mathscr{C}$ and direction set $\mathscr{D}$ of the extended normal cone inclusion friction law.

Experimental Setup

Various kinds of experimental setups to measure friction forces are used in the field of tribology. Such experiments utilize linear or rotational motion with a constant or oscillating sliding velocity. Point, line and flat contact areas are usually studied. Most conventional tribometers measure the friction force solely in the direction of sliding, even if anisotropic frictional behavior is considered (e.g., [72]). The findings of Sect. 5.1, however, show that if anisotropic friction forces are expected, it is not sufficient to measure the force in just one direction, as the friction force is not collinear with the sliding direction. The frictional behavior can only be analyzed accurately by measuring the forces in two directions in the contact plane, for different sliding directions.

In this work, an experimental setup consisting of a turning anisotropic surface and a stationary pin (pin-on-disk tribometer) is utilized [71]. In contrast to many

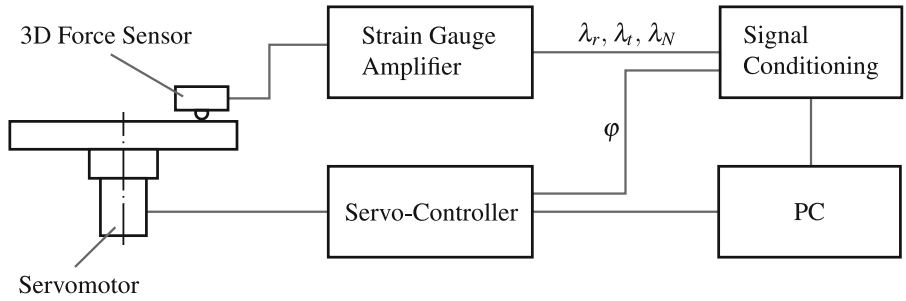

Fig. 21 Schematic diagram of the experimental setup

tribometers, friction forces are measured in two orthogonal directions and the rotation angle of the disk is recorded. During one full rotation of the disk, the friction forces for all possible sliding directions are observed. The pin-on-disk setup is shown in Fig. 20. The rotating disk has a diameter of 30 cm. It is driven with a synchronous servomotor with an integrated resolver and a harmonic drive gear such that the maximum speed of the disk is 200 rpm. The normal force is applied using weights that are placed on a linear ball spline shaft. The friction forces in tangential and radial direction of the disk, as well as the normal force are measured using a 3D force sensor. A schematic diagram of the experimental setup is shown in Fig. 21.

The tested pins have hemispherical or cylindrical shapes (diameter d_P) with a maximum diameter of 7 mm, resulting in a maximum apparent contact area of 38 mm^2. The position of the pin in radial direction of the rotating disk, denoted by r_P, is variable in the range from 60 to 149 mm and is constant during a measurement. The ratio between the diameter and radial position of the pin is chosen such that $d_P/r_P \ll 1$. Thus, the influence of varying sliding velocities along the radius of the disk, which leads to combined sliding and drilling friction, is minimized. For a given position, the relative sliding velocity is adjusted by the rotation speed of the disk.

During a measurement, the time signals of the friction forces in radial and tangential direction, the normal force, and the rotation angle of the disk are recorded.

Signal Processing

The output signals $\boldsymbol{F} = \begin{bmatrix} F_x & F_y & F_z \end{bmatrix}^{\mathrm{T}}$ of the force sensor do not directly correspond to the components of the contact force $\boldsymbol{\lambda} = [\lambda_r \ \lambda_t \ \lambda_N]^{\mathrm{T}}$ in radial, tangential, and normal direction. Crosstalk in multi-axis sensors produces an output signal in channels that do not correlate with the direction of the applied load. To minimize the effect, a compensation matrix $\boldsymbol{T}$ is used to transform the channel output into the reference frame of the sensor, i.e., $\boldsymbol{\lambda} = \boldsymbol{T}\boldsymbol{F}$. The matrix is determined by applying known loads using weights in each of the reference directions and calculating the inverse of the matrix consisting of the measured values. For the sensor used in this work, the matrix $\boldsymbol{T}$ is close to the identity matrix but has nonzero off-diagonal terms. The measured signals are filtered using a zero-phase low-pass Butterworth filter. With the obtained data, it is possible to determine the shapes of the force reservoir $\mathscr{C}$ and direction set $\mathscr{D}$ that define the extended normal cone inclusion friction law (see Definition 16). The friction forces λ_r and λ_t are measured in the I-frame of the sensor in radial and tangential direction of the disk (see Fig. 22a). With the measured current rotation angle φ of the disk, the forces can be transformed into the co-rotating frame K of the disk such that

$$\begin{bmatrix} -\lambda_{T_1} \\ -\lambda_{T_2} \end{bmatrix} = \begin{bmatrix} \cos\varphi & -\sin\varphi \\ \sin\varphi & \cos\varphi \end{bmatrix} \begin{bmatrix} \lambda_t \\ \lambda_r \end{bmatrix}, \tag{119}$$

Plotting the transformed forces in a diagram gives discrete points on the boundary of the force reservoir $\mathscr{C}$. The friction law defines the sliding direction by normality to the set $\mathscr{D}$. In the described experimental setup, the relative sliding velocity is known to point in tangential direction of the rotating disk. In the K-frame the vector $\boldsymbol{\gamma}_T$ can therefore be expressed as

$$\boldsymbol{\gamma}_T = \|\boldsymbol{\gamma}_T\| \begin{bmatrix} \cos\varphi \\ \sin\varphi \end{bmatrix}. \tag{120}$$

We address points on the boundary of $\mathscr{D}$ with the vector $\boldsymbol{r}_{\mathscr{D}}$ as shown in Fig. 22b. With the magnitude $r_{\mathscr{D}}$ and $\tan\theta = \lambda_{T_2}/\lambda_{T_1}$, the vector $\boldsymbol{r}_{\mathscr{D}}$ can be expressed in the K-frame as a function of θ,

$$\boldsymbol{r}_{\mathscr{D}}(\theta) = r_{\mathscr{D}}(\theta) \begin{bmatrix} \cos\theta \\ \sin\theta \end{bmatrix}. \tag{121}$$

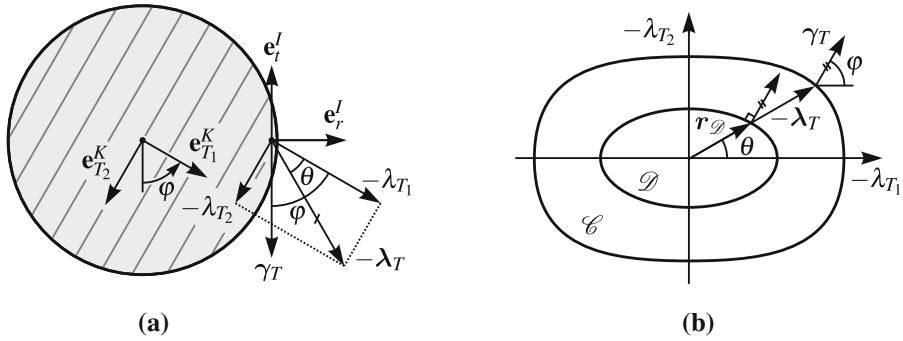

Fig. 22 **a** Top view of the rotating disk with coordinate frames. **b** Calculated sets $\mathscr{C}$ and $\mathscr{D}$

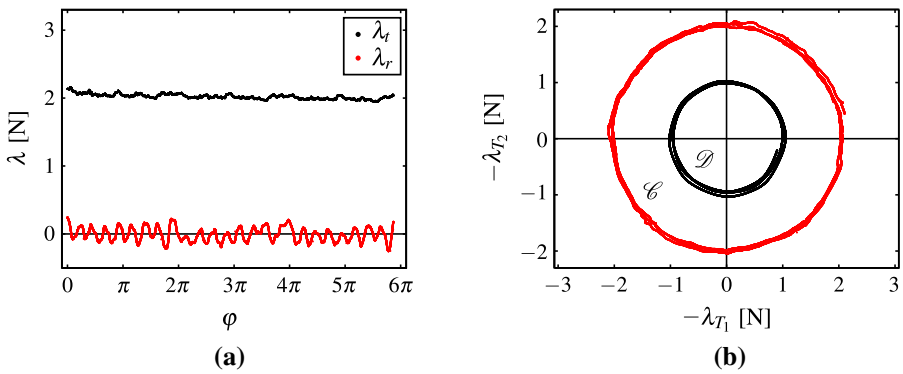

Fig. 23 Experimental results for steel pin on sandblasted steel disk. **a** Measured friction forces in tangential and radial direction. **b** Calculated sets $\mathscr{C}$ and $\mathscr{D}$

Its derivative with respect to θ,

$$\frac{\mathrm{d}\boldsymbol{r}_{\mathscr{D}}(\theta)}{\mathrm{d}\theta} := \boldsymbol{r}'_{\mathscr{D}}(\theta) = \begin{bmatrix} r'_{\mathscr{D}}(\theta)\cos\theta - r_{\mathscr{D}}(\theta)\sin\theta \\ r'_{\mathscr{D}}(\theta)\sin\theta + r_{\mathscr{D}}(\theta)\cos\theta \end{bmatrix}, \tag{122}$$

is tangential to the boundary of the set $\mathscr{D}$. Since $\boldsymbol{\gamma}_T$ is normal to $\mathscr{D}$, the condition

$$\boldsymbol{r}'_{\mathscr{D}}(\theta) \perp \boldsymbol{\gamma}_T \quad \Longleftrightarrow \quad \boldsymbol{r}'_{\mathscr{D}}(\theta) \cdot \boldsymbol{\gamma}_T = 0 \tag{123}$$

has to be met. Substitution of Eqs. (120) and (122) into the scalar product for $\|\boldsymbol{\gamma}_T\| \neq 0$ yields the first-order homogeneous differential equation

$$r'_{\mathscr{D}}(\theta) - \tan(\theta - \varphi) r_{\mathscr{D}}(\theta) = 0. \tag{124}$$

for the magnitude of $\boldsymbol{r}_{\mathscr{D}}$. From Fig. 22a, the relation $\tan(\theta - \varphi) = \lambda_r / \lambda_t$ is obtained. A solution of Eq. (124) is found by separation of variables and integration giving

$$r_{\mathscr{D}}(\theta) = r_{\mathscr{D}}(0) \mathrm{e}^{\int_0^\theta \frac{\lambda_r}{\lambda_t} \mathrm{d}\tilde{\theta}}. \tag{125}$$

As described in Sect. 3.4, the set $\mathscr{D}$ must be scaled such that $\mathscr{D} \subseteq \mathscr{C}$. This is achieved by choosing an appropriate initial value $r_{\mathscr{D}}(0)$. With the measured values of one full rotation of the disk, the sets $\mathscr{C}$ and $\mathscr{D}$ can be experimentally determined.

Experimental Results

The experimental setup can be used to measure the friction forces for various material combinations and surface conditions. All experiments are conducted under room temperature ($20 - 22°$) and in the unlubricated state. Before anisotropy is examined, a sample with a frictional behavior that is expected to be isotropic is analyzed.

Choosing a material and surface condition to represent *isotropic* frictional behavior is challenging since most surfaces show a surface texture that has an influence on the frictional properties. In this work, a sandblasted steel disk is considered. A hemispherical steel pin is pressed against the disk with a normal force of $\lambda_N = 14.0\,\mathrm{N}$. The relative sliding velocity depends on the rotation speed of the disk and the pin position in radial direction of the disk. It is set to $\|\boldsymbol{\gamma}_T\| = 50\,\mathrm{mm/s}$. The measured friction forces in tangential and radial direction, λ_t and λ_r, are shown in Fig. 23a. The tangen-

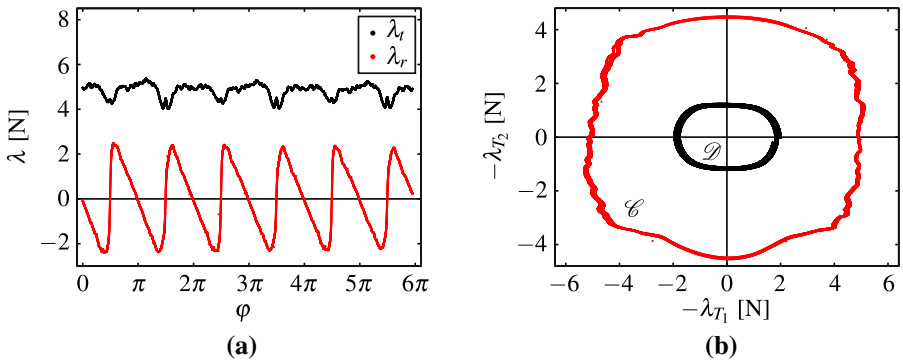

Fig. 24 Experimental results for PVC pin on surface ground steel disk. **a** Measured friction forces in tangential and radial direction. **b** Calculated sets $\mathscr{C}$ and $\mathscr{D}$

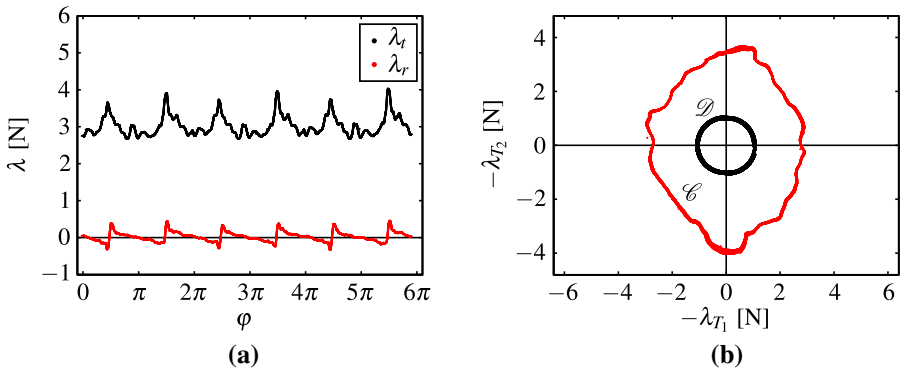

Fig. 25 Experimental results for steel pin on surface ground steel disk. **a** Measured friction forces in tangential and radial direction. **b** Calculated sets $\mathscr{C}$ and $\mathscr{D}$

tial force is constant, whereas the radial force is approximately zero. Small deviations are caused by irregularities of the surface. As expected for an isotropic material, the calculated sets $\mathscr{C}$ and $\mathscr{D}$ shown in Fig. 23b are circular. Therefore, isotropic frictional behavior can be described with the associated Coulomb friction law with a circular force reservoir (see Eq. 33). Since the magnitude of the friction force is independent of the sliding direction, a single value for the friction coefficient can be determined as $\mu \approx 0.14$.

An example of an *anisotropic* surface is given by a surface ground steel disk. Experiments with two different contact partners are conducted. Each measurement starts when the sliding direction is orthogonal to the grinding grooves. In Fig. 24a, the results for a cylindrical PVC pin with a diameter of 7 mm are shown. The experiment is performed with a normal force of $\lambda_N = 9.3\,\mathrm{N}$ and a sliding velocity of $\|\boldsymbol{\gamma}_T\| = 50\,\mathrm{mm/s}$. The friction forces exhibit a periodicity with two maxima per full rotation of the disk. This indicates an orthotropic frictional behavior which is expected for the surface ground disk due to symmetry. The tangential force component oscillates around a constant offset, while the radial force component shows a sawtooth oscillation around zero. A similar behavior is found by [22] for a different material combination. Maximum and minimum values of the tangential force occur at zero crossings of the radial force. For $\varphi = k\pi$, where $k \in \mathbb{N}$, the pin is sliding orthogonal to the grinding grooves and the tangential force is maximal. When the pin is sliding along the grooves, the tangential force is minimal. This behavior can be explained by the fact that PVC is softer than steel and adapts to the grinding grooves which hinders movement across the grooves. The resulting sets are shown in Fig. 24b. The force component orthogonal to the grooves is λ_{T_1}, whereas λ_{T_2} points in the direction of the grooves. The sets significantly differ from the circular shape in the isotropic case. Both sets are similar to rounded rectangles. A standard ellipse, as is often assumed for the force reservoir in the case of anisotropic friction in the literature, does not accurately describe the experimentally determined sets. The friction coefficients for sliding directions orthogonal and parallel to the grinding grooves are $\mu_1 \approx 0.54$ and $\mu_2 \approx 0.48$, respectively.

In addition to the measurements with a cylindrical PVC pin, experiments using a hemispherical steel pin are conducted. The results obtained using a nor-

mal force of $\lambda_N = 18.5\,\mathrm{N}$ and a sliding velocity of $\|\boldsymbol{\gamma}_T\| = 100\,\mathrm{mm/s}$ are shown in Fig. 25a. Again, the tangential component oscillates around a nonzero mean value, while the radial component shows a sawtooth behavior. However, note that for the steel pin, the maximum values of the tangential force occur when the pin is sliding along the grinding grooves. This behavior agrees with results found in the literature. Measurements performed by [73] show a higher friction coefficient along the grinding grooves than in orthogonal direction for a steel ball on a surface ground steel plate under lubricated conditions. Similar results are obtained by [74] under dry conditions for a steel plate with narrow groove-shaped textures. A physical explanation might be a higher stiffness of the ridges between the grooves in the longitudinal direction. The higher stiffness hinders deformation and motion of the pin in the direction parallel to the grinding grooves.

While in the literature usually only sliding along or across the grooves is regarded, the present study considers all sliding directions. The calculated sets are shown in Fig. 25b. The shapes of $\mathscr{C}$ and $\mathscr{D}$ substantially differ from each other. This behavior can not be represented by an associated friction law. The extended normal cone inclusion friction law, however, gives an accurate description of the frictional behavior.

5.3 Experimental validation of the friction law

The experiments described in the previous sections allow for an experimental validation of the extended normal cone inclusion friction law. From the measured friction forces of the contact pair PVC—surface ground steel, the force reservoir $\mathscr{C}$ and direction set $\mathscr{D}$ can be derived. The experimentally determined sets in combination with the friction law are used for a numerical simulation of a disk sliding on an anisotropic surface. The result can be directly compared to the experimentally obtained sliding path for the same material combination and initial condition.

Table 1 Semi-axes parameters and roundness factors of fitted sets

Set	Semi-major	Semi-minor	Roundness
Ellipsoidal $\mathscr{C}$	5.00 N	4.49 N	2
Superellipsoidal $\mathscr{C}$	4.99 N	4.25 N	2.94
Superellipsoidal $\mathscr{D}$	1.84	1.19	2.51

Often only the friction coefficients in the directions orthogonal and parallel to the grinding grooves are known and an ellipsoidal force reservoir $\mathscr{C}$ is assumed. Figure 26a shows such a set for the measured values of the PVC pin on the surface ground disk (see Fig. 24b)). A better fit of the measured values is obtained with the method of least squares for a superellipsoidal set as shown in Fig. 26b. In addition, a fit for the set $\mathscr{D}$ is plotted in Fig. 26c. The parameters of the sets are given in Table 1.

The experimentally determined sets are used for numerical simulations with different friction laws. The associated friction law is considered with the ellipsoidal and superellipsoidal force reservoir. The collinear friction law is formulated in combination with the superellipsoidal set. Finally, the extended normal cone inclusion friction law with two superellipsoidal sets is considered. The graphical representation of the friction laws is shown in Fig. 26. Numerical simulations of a sliding disk are performed with the time-

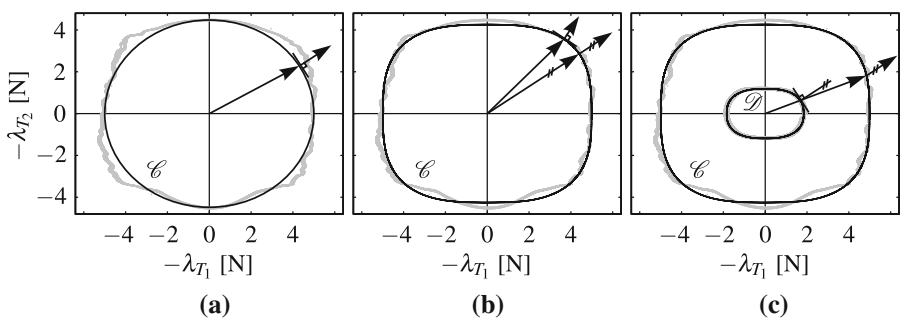

Fig. 26 Graphical representation of friction laws with fitted force reservoirs $\mathscr{C}$ and direction set $\mathscr{D}$ for measured friction forces of PVC on surface ground steel. **a** Associated friction law with ellipsoidal $\mathscr{C}$. **b** Associated and collinear friction law with superellipsoidal $\mathscr{C}$. **c** Extended normal cone inclusion friction law with superellipsoidal $\mathscr{C}$ and $\mathscr{D}$

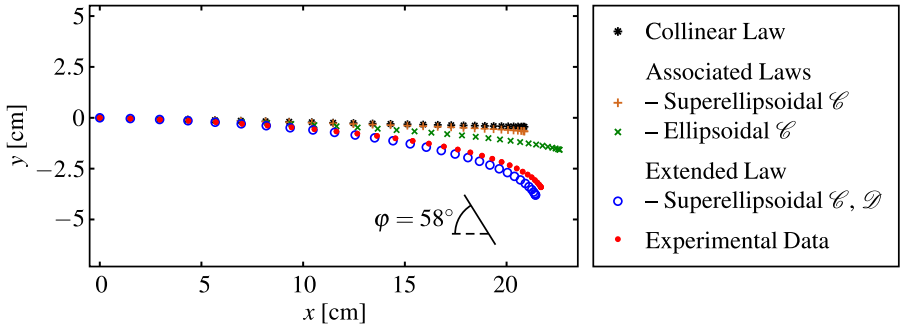

Fig. 27 Measured sliding path of PVC disk on surface ground steel and numerically obtained sliding paths using different friction laws with parameters from friction force measurement

stepping method explained in Sects. 2.3 and 3.4. The initial sliding velocity $v_0 = 1.52$ m/s and the orientation of the semi-axes with respect to the initial sliding direction $\varphi = 58°$ agree with the parameters of a measured sliding path of a PVC disk. The results are plotted in Fig. 27. Note that for reasons of clarity, only every fifth data point of the measured sliding path is plotted. The time between two plotted data points is 10 ms.

The results show a very good agreement of the measured sliding path and the path obtained with the extended law. Both length and deflection of the sliding path are similar. For the other friction laws, the deflection of the sliding path is much smaller. The collinear friction law obviously causes no deflection at all.

6 Conclusions

This work contributes to three research fields: modeling and simulation of nonsmooth mechanical systems, friction-induced instability and experimental analysis of anisotropic frictional behavior. It has been shown that all associated friction laws, i.e., friction laws characterized by normality of the sliding direction to the set of admissible friction forces are dissipative and that for a given force reservoir the associated flow rule maximizes the rate of dissipation. Different frictional behavior can be described by various shapes of the constant force reservoir. However, associated friction laws are limited to convex force reservoirs. Motivated by the study of non-associated frictional behavior found in the literature, in this work an extended normal cone inclusion friction law has been formulated using tools of convex analysis. The force law enables the description of set-valued anisotropic friction laws with possibly non-convex but star-shaped force reservoirs. The mathematical framework allows for the direct implementation of the force law in efficient numerical time-stepping schemes.

Furthermore, the stability of systems with anisotropic friction has been analyzed. From the maximal monotonicity of the associated Coulomb friction law, it follows that the law is unable to cause instability of an equilibrium. However, an eigenvalue analysis has proven that the extended normal cone inclusion law can lead to anisotropic friction-induced instability if the sliding direction is in the tangent cone of the force reservoir.
This is impossible for collinear force laws but can occur even for convex force reservoirs. Anisotropic friction-induced instability is a novel instability phenomenon that potentially occurs in systems with constant normal force and no dependence on the magnitude of the sliding velocity.

Finally, two experimental setups for the study of anisotropic frictional behavior have been proposed. Using a high-speed camera, it has been shown that, in general, a disk sliding on an anisotropic surface is deflected. This is caused by anisotropic friction forces that are not acting parallel to the sliding direction. In addition, friction forces have been measured in two orthogonal directions with a pin-on-disk tribometer. The described experimental procedure and data processing method allow for the visualization of the friction force reservoir for different contact pairs and surface conditions. Complex shapes of the force reservoir and no normality of the sliding direction to the force reservoir have been found. The experimental results have confirmed the benefit of the extended normal cone inclusion friction law.

Compliance with ethical standards

Conflict of interest The authors declare that they have no conflict of interest.

References

1. Coulomb, C.A.: Théorie des machines simples en ayant égard au frottement de leurs parties et à la roideur des cordages. Bachelier, Paris (1821)
2. Popova, E., Popov, V.L.: The research works of Coulomb and Amontons and generalized laws of friction. Friction **3**(2), 183–190 (2015)
3. Johnson, K.L.: Contact Mechanics. Cambridge University Press, Cambridge (1985)
4. van de Vrande, B.L., van Campen, D.H., de Kraker, A.: An approximate analysis of dry-friction-induced stick-slip vibrations by a smoothing procedure. Nonlinear Dyn. **19**(2), 159–171 (1999)
5. Glocker, Ch.: Set-Valued Force Laws: Dynamics of Non-Smooth Systems. Lecture Notes in Applied Mechanics, vol. 1. Springer, Berlin (2001)
6. Filippov, A.F.: Differential Equations with Discontinuous Right hand Sides. Kluwer Academic Publishers, Dordrecht (1988)
7. Rockafellar, R.T.: Convex Analysis. Princeton Landmarks in Mathematics. Princeton University Press, Princeton (1970)
8. Rockafellar, R.T., Wets, R.J.B.: Variational Analysis. Springer, Berlin (1998)
9. Aubin, J.P., Cellina, A.: Differential Inclusions: Set-Valued Maps and Viability Theory. Grundlehren der mathematischen Wissenschaften, vol. 264. Springer, Berlin (1984)
10. Clarke, F.H., Ledyaev, Y.S., Stern, R.J., Wolenski, P.R.: Nonsmooth Analysis and Control Theory. Graduate Texts in Mathematics, vol. 178. Springer, New York (1998)
11. Jean, M.: The non-smooth contact dynamics method. Comput. Method Appl. Mech. Eng. **177**(3), 235–257 (1999)
12. Moreau, J.J.: Unilateral contact and dry friction in finite freedom dynamics. In: Moreau, J.J., Panagiotopoulos, P.D. (eds.) Nonsmooth Mechanics and Applications. CISM Courses and Lectures, vol. 302, pp. 1–82. Springer, Wien (1988)
13. Acary, V., Brogliato, B.: Numerical Methods for Nonsmooth Dynamical Systems: Applications in Mechanics and Electronics. Lecture Notes in Applied and Computational Mechanics, vol. 35. Springer, Berlin (2008)
14. Leine, R.I., Nijmeijer, H.: Dynamics and Bifurcations of Non-Smooth Mechanical Systems. Lecture Notes in Applied and Computational Mechanics, vol. 18. Springer, Berlin (2004)
15. Zmitrowicz, A.: Models of kinematics dependent anisotropic and heterogeneous friction. Int. J. Solids. Struct. **43**(14), 4407–4451 (2006)
16. Menezes, P.L., Kishore, K.S.V., Lovell, M.R.: Role of surface texture, roughness, and hardness on friction during unidirectional sliding. Tribol. Lett. **41**(1), 1–15 (2011)
17. Saha, P.K., Wilson, W.R., Timsit, R.S.: Influence of surface topography on the frictional characteristics of 3104 aluminum alloy sheet. Wear **197**(1–2), 123–129 (1996)
18. Liu, X., Liewald, M., Becker, D.: Effects of rolling direction and lubricant on friction in sheet metal forming. J. Tribol. **131**(4), 042101 (2009). 1–8
19. Rabinowicz, E.: Direction of the friction force. Nature **179**, 1073 (1957)
20. Halaunbrenner, M.: Directional effects in friction. Wear **3**(6), 421–425 (1960)
21. Konyukhov, A., Vielsack, P., Schweizerhof, K.: On coupled models of anisotropic contact surfaces and their experimental validation. Wear **264**(7), 579–588 (2008)
22. Tapia, F., Le Tourneau, D., Géminard, J.C.: Anisotropic friction: assessment of force components and resulting trajectories. EPJ Tech. Instrum. **3**(1), 1–10 (2016)
23. Goyal, S.: Planar sliding of a rigid body with dry friction: limit surfaces and dynamics of motion. Ph.D. thesis, Cornell University (1989)
24. Michalowski, R., Mróz, Z.: Associated and non-associated sliding rules in contact friction problems. Arch. Mech. **30**(3), 259–276 (1978)
25. Mróz, Z., Stupkiewicz, S.: An anisotropic friction and wear model. Int. J. Solids Struct. **31**(8), 1113–1131 (1994)
26. de Saxcé, G., Feng, Z.Q.: New inequality and functional for contact with friction: the implicit standard material approach. J. Struct. Mech. **19**(3), 301–325 (1991)
27. Hjiaj, M., Feng, Z.Q., de Saxcé, G., Mróz, Z.: Three-dimensional finite element computations for frictional contact problems with non-associated sliding rule. Int. J. Numer. Method Eng. **60**(12), 2045–2076 (2004)
28. Zmitrowicz, A.: Mathematical descriptions of anisotropic friction. Int. J. Solids Struct. **25**(8), 837–862 (1989)
29. He, Q.C., Curnier, A.: Anisotropic dry friction between two orthotropic surfaces undergoing large displacements. Eur. J. Mech. A/Solids **12**(5), 631–666 (1993)
30. Transeth, A.A., Leine, R.I., Glocker, Ch., Pettersen, K.Y.: 3-D snake robot motion: nonsmooth modeling, simulations, and experiments. IEEE Trans. Robot. **24**(2), 361–376 (2008)
31. Arnold, P.D.: Analyse und Konzeption von Bobfahrwerken. Ph.D. thesis, ETH Zurich (2013)
32. Feeny, B., Guran, A., Hinrichs, N., Popp, K.: A historical review on dry friction and stick-slip phenomena. Appl. Mech. Rev. **51**(5), 321–342 (1998)
33. Ibrahim, R.A.: Friction-induced vibration, chatter, squeal, and chaos, part ii: dynamics and modeling. ASME Appl. Mech. Rev. **47**(7), 227–253 (1994)
34. Spurr, R.T.: A theory of brake squeal. Proc. Inst. Mech. Eng. Autom. Div. **15**(1), 33–52 (1961)
35. Hoffmann, N., Fischer, M., Allgaier, R., Gaul, L.: A minimal model for studying properties of the mode-coupling type instability in friction induced oscillations. Mech. Res. Commun. **29**(4), 197–205 (2002)
36. Wallaschek, J., Hach, K.H., Stolz, U., Mody, P.: A survey of the present state of friction modelling in the analytical and numerical investigation of brake noise generation. In: Proceedings of the ASME Vibration Conference, Las Vegas, Nevada (1999)
37. Kinkaid, N.M., O'Reilly, O.M., Papadopoulos, P.: Automotive disc brake squeal. J. Sound Vib. **267**(1), 105–166 (2003)
38. von Wagner, U., Hochlenert, D., Hagedorn, P.: Minimal models for disk brake squeal. J. Sound Vib. **302**(3), 527–539 (2007)
39. Ghazaly, N.M., El-Sharkawy, M., Ahmed, I.: A review of automotive brake squeal mechanisms. J. Mech. Des. Vib. **1**(1), 5–9 (2013)
40. Hetzler, H.: Zur Stabilität von Systemen bewegter Kontinua mit Reibkontakten am Beispiel des Bremsenquietschens. Ph.D. thesis, Universität Karlsruhe (TH) (2008)

41. Brogliato, B.: Nonsmooth Mechanics: Models, Dynamics and Control, 3rd edn. Springer, Switzerland (2016)
42. Leine, R.I., van de Wouw, N.: Stability and Convergence of Mechanical Systems with Unilateral Constraints. Lecture Notes in Applied and Computational Mechanics, vol. 36. Springer, Berlin (2008)
43. Demyanov, V.F., Stavroulakis, G.E., Polyakova, L.N., Panagiotopoulos, P.D.: Quasidifferentiability and Nonsmooth Modelling in Mechanics, Engineering and Economics, Nonconvex Optimization and Its Applications, vol. 10. Springer, Dordrecht (1996)
44. Möller, M., Leine, R.I., Glocker, Ch.: An efficient approximation of orthotropic set-valued force laws of normal cone type. In: Proceedings of the 7th Euromech Solid Mechanics Conference, Lisbon, Portugal (2009)
45. Clarke, F.H., Aubin, J.P.: Monotone invariant solutions to differential inclusions. J. Lond. Math. Soc. **2**(2), 357–366 (1977)
46. Alart, P., Curnier, A.: A mixed formulation for frictional contact problems prone to Newton like solution methods. Comput. Method Appl. Mech. Eng. **92**(3), 353–375 (1991)
47. Moreau, J.J.: Application of convex analysis to some problems of dry friction. In: Zorski, H. (ed.) Trends in Applications of Pure Mathematics to Mechanics, vol. 2, pp. 263–280. Pitman Publishing Ltd, London (1979)
48. Baumann, M.: Synchronization of nonsmooth mechanical systems with impulsive motion. Ph.D. thesis, ETH Zurich (2017)
49. Leine, R.I., Glocker, Ch.: A set-valued force law for spatial Coulomb–Contensou friction. Eur. J. Mech. A/Solids **22**(2), 193–216 (2003)
50. Saito, M., Fukaya, M., Iwasaki, T.: Modeling, analysis, and synthesis of serpentine locomotion with a multilink robotic snake. IEEE Control Syst. Mag. **22**(1), 64–81 (2002)
51. Rempfler, G.S., Glocker, Ch.: A bobsleigh simulator software. Multibody Syst. Dyn. **36**(3), 257–278 (2016)
52. Liewald, M., Wagner, S., Becker, D.: New approaches on Coulomb's friction model for anisotropic sheet metal forming applications. In: Proceedings of the 9th ESAFORM Conference on Material Forming, Glasgow (2006)
53. Hjiaj, M., Feng, Z.Q., de Saxcé, G., Mróz, Z.: On the modelling of complex anisotropic frictional contact laws. Int. J. Eng. Sci. **42**(10), 1013–1034 (2004)
54. Hjiaj, M., de Saxcé, G., Mróz, Z.: A variational inequality-based formulation of the frictional contact law with a non-associated sliding rule. Eur. J. Mech. A/Solids **21**(1), 49–59 (2002)
55. de Saxcé, G., Feng, Z.Q.: The bipotential method: a constructive approach to design the complete contact law with friction and improved numerical algorithms. Math. Comput. Model. **28**(4), 225–245 (1998)
56. Zmitrowicz, A.: Constitutive modelling of anisotropic phenomena of friction, wear and frictional heat. Studia i Materiały, vol. 381/1342/93 Instytut Maszyn Przepływowych PAN, Gdańsk (1993)
57. Walker, S.V., Leine, R.I.: Modeling and numerical simulation of anisotropic dry friction with non-convex friction force reservoir. In: Proceedings of the 4th Joint International Conference on Multibody System Dynamics (IMSD 2016), Montréal, Canada (2016)
58. Leine, R.I., Brogliato, B., Nijmeijer, H.: Periodic motion and bifurcations induced by the Painlevé paradox. Eur. J. Mech. A/Solids **21**(5), 869–896 (2002)
59. Leine, R.I., van Campen, D.H., de Kraker, A., van den Steen, L.: Stick-slip vibrations induced by alternate friction models. Nonlinear Dyn. **16**(1), 41–54 (1998)
60. Popp, K., Stelter, P.: Stick-slip vibrations and chaos. Philos. Trans. Phys. Sci. Eng. **332**, 89–105 (1990)
61. Hetzler, H., Schwarzer, D., Seemann, W.: Analytical investigation of steady-state stability and Hopf-bifurcations occurring in sliding friction oscillators with application to low-frequency disc brake noise. Commun. Nonlin. Sci. Numer. Simul. **12**(1), 83–99 (2007)
62. Hoffmann, N., Gaul, L.: Effects of damping on mode-coupling instability in friction induced oscillations. Zeitschrift für Angewandte Mathematik und Mechanik **83**(8), 524–534 (2003)
63. Sinou, J.J., Jezequel, L.: Mode coupling instability in friction-induced vibrations and its dependency on system parameters including damping. Eur. J. Mech. A/Solids **26**(1), 106–122 (2007)
64. Hoffmann, N., Gaul, L.: A sufficient criterion for the onset of sprag-slip oscillations. Arch. Appl. Mech. **73**(9), 650–660 (2004)
65. Painlevé, P.: Sur les lois du frottement de glissement. Comptes Rendu des Séances de l'Academie des Sciences **121**, 112–115 (1895)
66. Ouyang, H., Mottershead, J.E., Cartmell, M.P., Friswell, M.I.: Friction-induced parametric resonances in discs: effect of a negative friction–velocity relationship. J. Sound. Vib. **209**(2), 251–264 (1998)
67. Bigoni, D., Noselli, G.: Experimental evidence of flutter and divergence instabilities induced by dry friction. J. Mech. Phys. Solids **59**(10), 2208–2226 (2011)
68. Brogliato, B., Goeleven, D.: Well-posedness, stability and invariance results for a class of multivalued Lur'e dynamical systems. Nonlin. Anal. Theory Method Appl. **74**(1), 195–212 (2011)
69. Müller, P.C.: Stabilität und Matrizen: Matrizenverfahren in der Stabilitätstheorie linearer dynamischer Systeme. Springer, Berlin (1977)
70. Khalil, H.K.: Nonlinear Systems, 3rd edn. Prentice Hall, Upper Saddle River (2002)
71. Walker, S.V., Leine, R.I.: Anisotropic dry friction with non-convex force reservoirs: modeling and experiments. In: Proceedings of the 9th European Nonlinear Dynamics Conference (ENOC 2017), Budapest, Hungary (2017)
72. Rhaiem, S., Dammak, M., Shirazi-Adl, A., Mesfar, W., Maalej, A.: Combined experimental and finite element studies of anisotropic friction. J. Mater. Sci. Technol. **20**, 11–14 (2004)
73. Singh, R., Melkote, S.N., Hashimoto, F.: Frictional response of precision finished surfaces in pure sliding. Wear **258**(10), 1500–1509 (2005)
74. Yu, C., Wang, Q.J.: Friction anisotropy with respect to topographic orientation. Sci. Rep. **2**(988), 1–6 (2012)